The Mercury Atmospheric and Surface Composition Spectrometer for the MESSENGER Mission

William E. McClintock · Mark R. Lankton

Abstract The Mercury Atmospheric and Surface Composition Spectrometer (MASCS) is one of seven science instruments onboard the MErcury Surface, Space ENvironment, GEochemistry, and Ranging (MESSENGER) spacecraft en route to the planet Mercury. MASCS consists of a small Cassegrain telescope with 257-mm effective focal length and a 50-mm aperture that simultaneously feeds an UltraViolet and Visible Spectrometer (UVVS) and a Visible and InfraRed Spectrograph (VIRS). UVVS is a 125-mm focal length, scanning grating, Ebert-Fastie monochromator equipped with three photomultiplier tube detectors that cover far ultraviolet (115–180 nm), middle ultraviolet (160–320 nm), and visible (250–600 nm) wavelengths with an average 0.6-nm spectral resolution. It will measure altitude profiles of known species in order to determine the composition and structure of Mercury's exosphere and its variability and will search for previously undetected exospheric species. VIRS is a 210-mm focal length, fixed concave grating spectrograph equipped with a beam splitter that simultaneously disperses the spectrum onto a 512-element silicon visible photodiode array (300–1050 nm) and a 256-element indium-gallium-arsenide infrared photodiode array 850–1,450 nm. It will obtain maps of surface reflectance spectra with a 5-nm resolution in the 300–1,450 nm wavelength range that will be used to investigate mineralogical composition on spatial scales of 5 km. UVVS will also observe the surface in the far and middle ultraviolet at a 10-km or smaller spatial scale. This paper summarizes the science rationale and measurement objectives for MASCS, discusses its detailed design and its calibration requirements, and briefly outlines observation strategies for its use during MESSENGER orbital operations around Mercury.

Keywords Atmosphere · Exosphere · Mercury · MESSENGER · Spectrometer · Surface

1 Introduction

The Mercury Atmospheric and Surface Composition Spectrometer (MASCS) is one of seven science instruments aboard the MErcury Surface, Space ENvironment, GEochemistry, and

W.E. McClintock (✉) · M.R. Lankton
Laboratory for Atmospheric and Space Physics, University of Colorado, Boulder, USA
e-mail: william.mcclintock@lasp.colorado.edu

Ranging (MESSENGER) spacecraft. It is designed to provide measurements that address four of the six science questions that frame the MESSENGER mission:

1. What planetary formation processes led to the high metal/silicate ratio in Mercury?
2. What is the geological history of Mercury?
3. What are the radar reflective materials at Mercury's poles?
4. What are the important volatile species and their sources and sinks on and near Mercury?

MASCS consists of a small Cassegrain telescope that simultaneously feeds a Visible and InfraRed Spectrograph (VIRS) and an UltraViolet and Visible Spectrometer (UVVS). It will obtain maps of surface reflectance spectra that will be used to investigate the mineralogical composition of the surface on spatial scales of 5 km or less. UVVS will measure altitude profiles of known species in order to determine composition and structure of the exosphere and its variability. It will also search for signatures of possible volatile polar deposits and previously undetected exospheric constituents.

2 Science Objectives

2.1 Exosphere

The atmosphere of Mercury is a surface-bounded exosphere, which acts as an interface between the surface and external stimuli impinging upon it (Killen and Ip 1999; Domingue et al. 2007). Its composition and behavior are controlled by its interactions with the magnetosphere and the surface. The MESSENGER exospheric science investigation is based upon four key questions related to the nature of the exosphere and its relationship to the external processes that modify the surface:

1. What are the composition, structure, and temporal behavior of the exosphere?
2. What are the processes that generate and maintain the exosphere?
3. What is the relationship between exospheric and surface composition?
4. Are there polar deposits of volatile material, and how are the accumulation of these deposits related to exospheric processes?

1. What are the composition, structure, and temporal behavior of the exosphere?
Mercury's exosphere is known to contain six elements (H, He, O, Na, Ca, and K) that taken together have a surface density at the subsolar point of approximately 10^4 atoms cm^{-3} (Hunten et al. 1988). The airglow spectrometer aboard the Mariner 10 flyby mission detected H, He, and O (Broadfoot et al. 1974a, 1974b). Potter and Morgan discovered Na and K using high-resolution ground-based spectroscopic observations (Potter and Morgan 1985, 1986). Bida et al. (2000) detected high-temperature Ca using the Keck I telescope. Searches for additional constituents have not been successful (Hunten et al. 1988).

Ground-based studies of Na indicate that the exosphere is spatially and temporally variable. There are orderly changes in Na surface density related to changes in solar radiation pressure and distance (Killen et al. 1990), but there are also chaotic variations in the exosphere. The subsolar Na density has been observed to change by a factor of two on time scales of less than a week, and bright Na emission spots have been observed at high northern latitudes and over the Caloris basin.

With the existing data our inventory of Mercury's exospheric composition is incomplete. Current understanding of the source processes (discussed later) suggests the presence of as yet undetected species including Ar, Si, Al, Mg, Fe, S, and OH (from impact vaporization of

H_2O). With the exception of Ar, all of the species listed above have strong ground-state emission lines (predicted intensities in the range 10–1,000 Rayleighs, e.g., Morgan and Killen 1996) in the spectral range 130–600 nm, but observational constraints have prevented us from detecting these species from the ground or from Earth-orbiting spacecraft.

The measurements required to support the investigation of Mercury's exospheric composition and structure are: (1) altitude profiles of known species (H, O, Na, Ca, and K) measured with a vertical resolution comparable to an exospheric scale height (25–50 km) and a latitude/longitude resolution of 10–20°, and (2) a sensitive search for predicted species that have not been previously observed (e.g., Si, Al, Mg, Fe, S, OH).

The UVVS channel of MASCS is specifically designed to make these measurements. It provides broad spectral coverage (115–600 nm), moderate spectral resolution (0.6 nm), and high sensitivity (detection limit ~100 Rayleighs), enabling it to produce a detailed inventory of the species in the exosphere of Mercury (or strong upper limits) together with the vertical and horizontal distributions of the most abundant species. In addition to determining composition and structure, these data will provide the basis for determining exospheric processes, studying the relationship between surface and exospheric composition, and studying surface–exosphere–magnetosphere interactions.

2. What are the processes that generate and maintain the exosphere?

The processes that supply and remove exospheric material have been identified, but their relative importance is poorly understood. Hydrogen and helium are likely derived from neutralized solar wind ions, although photodissociation of meteoritic water and crustal outgassing should supply a portion of these two species. Proposed sources for Na, K, Ca, and O include impact vaporization, ion sputtering, photon stimulated desorption, thermal desorption, and crustal degassing. Currently, there is strong disagreement about the relative importance of these four mechanisms (McGrath et al. 1986; Sprague 1990; Morgan and Killen 1996). Determining a comprehensive inventory of exospheric species and measuring their spatial and temporal distributions will allow us to quantify the dominant source mechanisms for the various exospheric species.

The principal loss mechanisms are thermal escape and photoionization with subsequent loss through transport along open magnetic field lines. Although thermal escape appears to be the dominant loss mechanism for both hydrogen and helium, it is probably unimportant for Na and K (Hunten et al. 1988). Photoionization rates for Na and K are relatively well known; however, the total loss rates from the exosphere are uncertain by a factor of ten because the efficiency with which ions are swept away by the convecting electric field is highly uncertain. Based on lunar studies (Mendillo et al. 1991), gas–surface interactions may also be an important sink for sodium and potassium.

UVVS measurements of composition and structure will provide the data required to characterize exospheric processes. Distributions for sodium and other species with strong emission lines will permit a definitive determination of their surface interaction. By understanding the interactions of the major species with the surface we can use the inventory to determine the relative importance of the key source processes.

Correlating UVVS data with Energetic Particle and Plasma Spectrometer (EPPS) (Andrews et al. 2007) and Magnetometer (Anderson et al. 2007) data will provide an additional tool for understanding exospheric processes. The magnetic field controls the location and strength of sputtering ion flux as well as the efficiency of photo-ion loss from the planet. By relating local variations in exospheric composition with the loci of charged particle precipitation on the surface, we can isolate sputtering as a source. Similarly, production rates from impact vaporization, which depend on the magnitude of impact velocity, should peak in the ram direction of Mercury's orbital motion.

We can also examine the importance of crustal outgassing and search for surface features (e.g., the Caloris basin, Sprague 1990; Sprague et al. 1998) that may be associated with enhanced concentrations of exospheric sodium or potassium. Establishing a convincing exosphere–basin correlation requires that we remove the contributions from all other effects, most of which are related to the magnetosphere, the solar wind, and changes in solar ultraviolet (UV) and extreme ultraviolet (EUV) flux.

In addition to neutral species, the UVVS should detect such prominent ions along lines of sight as Ca^+ and Mg^+, which pass over the poles and extend along the magnetotail. Strong resonance lines for S^+, Si^+, and Al^+ also fall in the spectral range of the UVVS. A measurement of an element in the exosphere and the corresponding ion in the tail will help us determine the rate at which ions are permanently lost from the planet.

3. What is the relationship between exospheric and surface composition?

Except for the noble gases, hydrogen, and a few volatile species such as sulfur, which are abundant in the micrometeoroid population, species found in the exosphere are thought to be derived from the regolith and crust. If we can quantify the sources, sinks, and gas–surface interactions of the exosphere, then measuring other regolith-derived elements (Ca, Mg, Al, Fe) will allow us to estimate the relative abundances of these species on the surface. For example, Morgan and Killen (1996) showed that if sputtering is the dominant source, then the relative abundances of Ca, Al, Fe, Mg, and Si in the exosphere are related to surface composition.

Exospheric detection, together with detection by the Gamma-Ray and Neutron Spectrometer (Goldsten et al. 2007) and by color imaging (Hawkins et al. 2007) and surface reflectance spectroscopy, provide the data required to support the correlation between exospheric and surface composition.

4. Are there polar deposits of volatile material, and how are the accumulation of these deposits related to exospheric processes?

One of the most exciting recent discoveries about Mercury comes from ground-based radar backscatter measurements that have been interpreted as arising from polar deposits of water ice on the surface or at shallow depths (Slade et al. 1992; Butler et al. 1993). An alternative interpretation was offered by Sprague et al. (1995), who concluded that the observations indicate deposits of elemental sulfur. In either case, one mechanism that may explain the accumulation of volatile species at the poles is impact vaporization of infalling material followed by exospheric transport to the poles and trapping in permanent shadows.

The UVVS will search for the presence of water ice deposits at the poles by measuring the distribution of the daughter product of water dissociation, the hydroxyl molecule (OH). Impact vaporization, sublimation, and degassing are expected to contribute water to the exosphere, where photodissociation by sunlight produces OH. Similar source mechanisms will also supply sulfur to the exosphere. Killen et al. (1997) calculated the expected exospheric concentration of OH from both buried and exposed ice deposits for a wide variety of surface conditions. They concluded that the OH surface density should exceed 10^3 cm^{-3} and that the OH emission rate at wavelength $\lambda = 306$ nm should be greater than 100 Rayleighs if the surface temperature is greater than about 110 K. This intensity is easily detectable by the UVVS. (Similar calculations for the sublimation and degassing rates for sulfur have not yet been completed; nonetheless, we expect that a surface density of 8×10^3 cm^{-3} would produce an emission strength of about 200 Rayleighs at $\lambda = 181.3$ nm, which would also be easily detected by the UVVS.)

Specifically, the MASCS exosphere measurement objectives are to provide exospheric composition over the polar regions and to make spectral measurements of exospheric composition and density as functions of latitude, time of solar day, and time of solar year.

2.2 Formation and Geological History

The MASCS instrument will also provide data to address MESSENGER science questions regarding the formation process of Mercury and its geological history:

1. What is the mineralogy of Mercury's surface and its variation with geological unit?
2. What is the rate of space weathering on Mercury, and how does it affect spectral interpretations?

1. What is the mineralogy of Mercury's surface and its variation with geological unit?

The mineralogical composition of Mercury's surface material is largely unknown. Although Earth-based observations indicate that the reflectance spectra of Mercury show similarity in shape and slope with those of the lunar highlands, it is recognized that the spectra of the two bodies also show a marked difference. Whereas the Moon's spectrum shows an absorption band near 1,000 nm caused by ferrous iron in pyroxenes and olivines (Adams and McCord 1970), Mercury's spectrum shows, at most, a weak, distorted feature near 1 μm, and evidence is accumulating that Mercury's surface is low in Fe^{2+} (Vilas 1985), limiting the average FeO content to less than about 3–6% by weight (Blewett et al. 1997). Further, Warell et al. (2006) argued that a broad feature near 1,000 nm recently observed at mid latitudes and 190°E longitude results from the presence of iron-poor, high-calcium clinopyroxene. Clementine UV–visible multispectral measurements have led to the identification of large regions on the lunar farside that are extremely low in FeO (<3% by weight) (Lucey et al., 1998, 2000a). Such areas are believed to be composed of >90% plagioclase feldspar. Furthermore, recent observations of the Moon have revealed small areas of the nearside that lack the otherwise ubiquitous 1-μm ferrous iron absorption band (Blewett et al. 2002, and references therein), leading to the possibility that Mercury's surface composition can be classified as pure anorthosite. In addition to anorthosite, there are alternative mineralogies for Mercury with featureless reflectance spectra. Earth-based mid-infrared observations show emission features consistent with the presence of both calcic plagioclase feldspar containing some sodium and very-low-FeO pyroxene (Sprague et al. 2002).

The current paradigm for Mercury, derived from Earth-based observations, suggests a crust composed predominantly of plagioclase feldspar (anorthitic to albitic) with little basaltic materials, showing virtually no large-scale compositional variation. However, Mariner 10 color data indicate the presence of several units, too small to be detected from Earth, thought to be enriched in opaque minerals (relatively low albedo and blue color) (Rava and Hapke 1987; Robinson and Lucey 1997; Robinson and Taylor 2001). Mercury's surface also contains an unknown proportion of meteoritic material, perhaps as much as 5–20% (Noble and Pieters 2003), which can provide nontypical constituents, such as sulfur or carbon. Spectral reflectance information obtained in the range 400–1,500 nm can identify key minerals and estimate their abundances. On the basis of results from Clementine lunar observations (Lucey 2004) the anticipated accuracy at Mercury should be on the order of 10% or better; although Warell and Blewett (2004) argued that differences in composition and rates of space weathering on Mercury and the Moon (Cintala 1992) may nullify many of the detailed retrieval algorithms for lunar materials (e.g. Lucey et al. 1998, 2000a, 2000b). Mariner 10 images also show regions with albedo differences that may indicate small variations in mafic minerals. Characterizing the major mineral constituents of Mercury's crust places important constraints on formation models of the planet.

Mariner 10 color images show that, despite the heavily agglutinized nature of the surface, many color differences exist that must be due to compositional rather than maturity differences. These units fall into three broad categories: first is the "average" Mercury surface, composed predominantly of the ancient heavily cratered terrain and intercrater plains.

Second, there is a relatively low-albedo, blue material that generally appears insensitive to local topographic undulations and exhibits feathered or indistinct margins. This material is possibly relatively rich in opaque mineral content and may have been emplaced in explosive eruptions (Robinson and Lucey 1997). Interestingly, several smooth plains units appear to embay and therefore postdate this unit. The color properties of the smooth plains are similar to the global average. Detailed spectral characterization of the smooth plains is a high priority for MASCS. Determining compositional variations within and between smooth plains deposits will give the best chance of understanding the evolution of the crust and the composition of Mercury's mantle (Robinson and Taylor 2001). Third, one of the more mysterious units seen in the Mariner 10 color images is a class of materials exhibiting high albedo and red color. These materials were noted in early papers as anomalous high-albedo patches in the floors of several craters (Dzurisin 1977). Similar to the Tycho crater on the Moon, a low-albedo annulus is present around the crater Basho.

2. What is the rate of space weathering on Mercury, and how does it affect spectral interpretation?

A serious obstacle to the interpretation of any spectral data for Mercury is the intense space weathering environment at Mercury's orbit, which results in a high percentage of the surface being converted to agglutinates or glass (Cintala 1992). Agglutinates tend to shift band centers, but more importantly they suppress band depths, thus making the identification of iron bands difficult—especially with FeO contents below 10% by weight. To overcome this problem a key MESSENGER strategy is the acquisition of spectra of as many Kuiperian (immature) ejecta blankets as possible. When an impact crater is formed, material from depth is excavated and deposited near the rim. Initially this material is nearly agglutinate free, but over time the space weathering process continually converts crystalline material to agglutinitic material, thus lowering the albedo, reddening the spectral slope, and suppressing absorption bands. Even if the true mineralogic properties of fully mature material cannot be recovered, the fresh ejecta blankets will provide a random sample of the local bulk composition. Lucey (2004) followed such a strategy with Clementine spectral data to produce an interpolated 1-km-per-pixel major mineralogy map of the Moon (clinopyroxene, orthopyroxene, olivine, plagioclase feldspar).

Specifically, the MASCS surface composition science measurement objectives will contribute to the goals of the MESSENGER geology investigation (Head et al. 2007) by providing spectral measurement of the surface mineralogy associated with Fe-bearing, Ti-bearing, and other units via visible and near-infrared absorption bands.

3 Measurement Requirements and Implementation

MASCS measurement requirements are summarized in Table 1. In general the MESSEN-GER mission design and launch vehicle selection severely limit both payload mass and data downlink volume. These considerations led to a design for an exospheric experiment that employs a scanning grating monochromator with photomultiplier tube detectors rather than one using fixed gratings and multielement detectors. The primary science objectives require a small, low-mass instrument with moderate resolution and very high sensitivity, which can measure a small number (10–20) of isolated emissions at known wavelengths spread over a very broad range. With the exception of the noble gasses, the known and predicted exospheric species have observable emission lines in the far ultraviolet to visible (115–600 nm). Noble gasses were excluded from the exosphere measurement objectives

Table 1 MASCS measurement requirements

Parameter	Atmospheric composition	Surface composition
Wavelength range	115–600 nm	115–1,450 nm
Spectral resolution	0.6 nm	5 nm
Spatial resolution	25-km height on limb	$<$500 µrad
	15–20° latitude/longitude	
Sensitivity	Detection of 10 Rayleighs in 100 s; $130 < \lambda < 425$ nm	Signal-to-noise >100

because their resonance lines lie in the extreme ultraviolet ($<$100 nm), requiring a separate optical train. Although most of these emissions are optically thin, the notable exception is the important sodium resonance doublet at 589.0 nm and 589.6 nm, which is optically thick for many observational geometries. Accurate retrieval of sodium column abundances requires that MASCS have sufficient spectral resolution to determine individual emission strengths of these two lines.

When the spectrum consists of a few isolated features, a scanner has a sensitivity advantage over a fixed grating design because it has very large light-gathering power per spectral resolution element. On the other hand, the requirement for simultaneous and continuous spectral coverage dictates the need for a fixed grating and multielement design for the visible and near-infrared surface reflectance measurements. Here, downlink limitations led to a point spectrograph rather than a mapping spectrograph design for surface composition studies. Obtaining visible and infrared spectra on a fixed latitude and longitude grid of 5 to 10 km instead of over a continuous swath will provide context for the full-coverage color images obtained with Mercury Dual Imaging System (Hawkins et al. 2007). Mercury thermal infrared emission limits the spectral coverage for reflectance spectroscopy to $<$1.5 µm, which is still adequate to measure signatures of ferrous oxide near 1 µm.

4 Instrument Description

4.1 Instrument Overview

Figure 1 is an image of the MASCS taken during instrument testing. The instrument consists of a small Cassegrain-style telescope simultaneously feeding both an Ultraviolet-Visible Spectrometer (UVVS) and a Visible-Infrared Spectrograph (VIRS). The telescope-UVVS configuration is nearly identical to the UltraViolet Spectrometer (UVS) aboard the Galileo spacecraft (Hord et al. 1992). It uses a plane-grating monochromator equipped with three photomultiplier tube (PMT) detectors to measure far ultraviolet (FUV-PMT, 115–190 nm), middle ultraviolet (MUV-PMT, 160–320 nm), and visible (VIS-PMT, 250–600 nm) wavelengths. Far ultraviolet wavelengths are observed in the second order of the grating with a typical resolution of 0.3 nm, while middle ultraviolet and visible wavelengths are observed in first order with resolutions that vary from 0.7 nm at 200 nm to 0.45 nm at 600 nm. UVVS is optimized for measuring the composition and structure of the exosphere and for measuring ultraviolet (wavelength $\lambda < 300$ nm) surface reflectance. VIRS is mounted on top of the UVVS and is coupled to the telescope focal plane with a short fiber optics bundle. It uses a fixed concave grating and two solid-state array detectors to measure visible (VIS, 300–1,050 nm) and near-infrared (NIR, 850–1,450 nm) wavelengths, both with a resolution

Fig. 1 MASCS instrument image taken during instrument testing at the Laboratory for Atmospheric and Space Physics (LASP) at the University of Colorado

of 4.7 nm (a dispersion of 2.33 nm per pixel). It is optimized for measuring visible and near-infrared ($0.3 \leq \lambda \leq 1.45$ μm) surface reflectance. A contamination door equipped with a MgF_2 window covers the telescope aperture. The MASCS control and interface electronics module, which uses a microprocessor-based logic system to manage instrument configuration, control UVVS spectral scanning, and provide spacecraft-instrument communications, is mounted on the side of the UVVS spectrometer housing. Figure 2 shows a functional block diagram that illustrates the instrument optical paths and electronic signal flow.

The UVVS will measure altitude profiles of known species (H, O, Na, K, and Ca), which will be used to determine exospheric temperature and density and to map the extended distributions of these species. It will make observations at a series of fixed wavelengths to search for predicted species that have not been previously detected (e.g., Si, Al, Mg, Fe, S, OH)
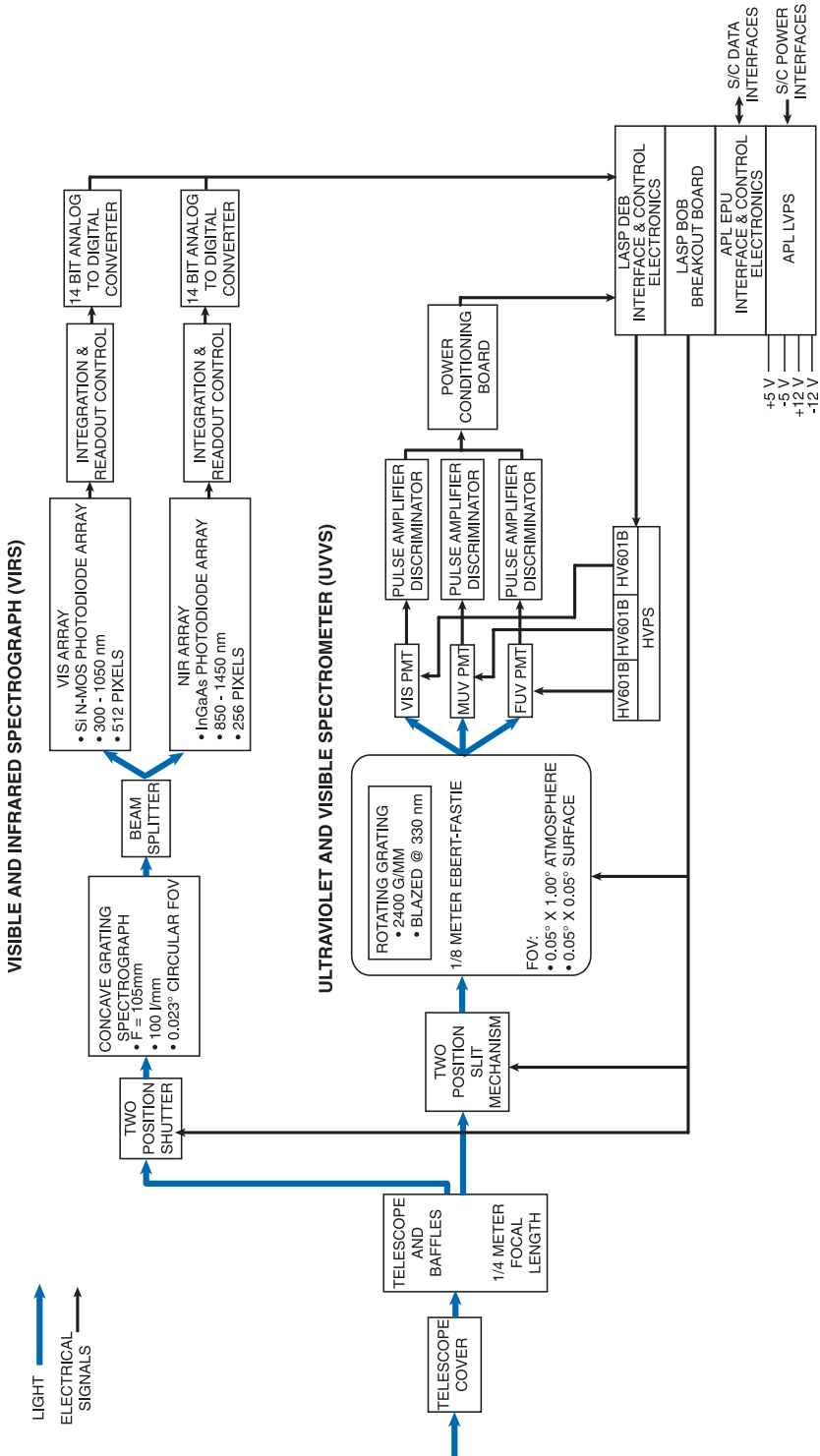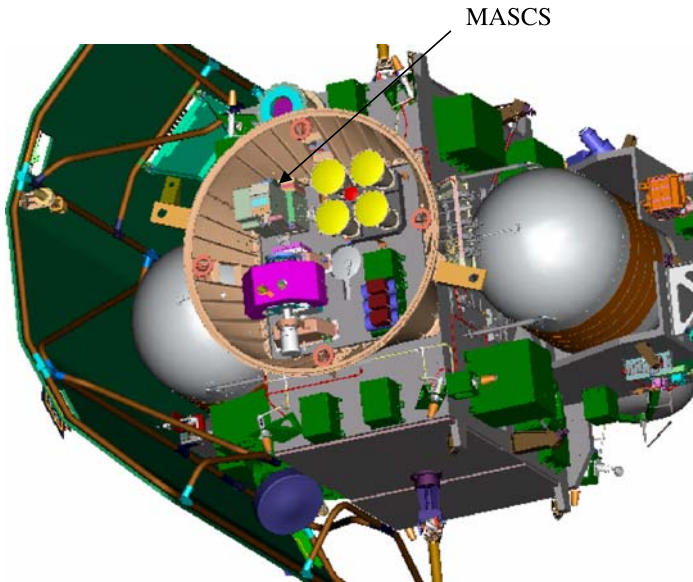
Fig. 2 MASCS functional block diagram showing optical paths and electronic signal flow

Fig. 3 MASCS (*arrow*) placement on the MESSENGER spacecraft aligns the telescope optic axis with the spacecraft +Z axis. For flight, thermal blankets cover the entire instrument except for the telescope aperture

and in spectral scans (115–600 nm) to search for new species (see Sect. 6.1). Together, the UVVS and VIRS will measure surface reflectance at middle ultraviolet to visible to near-infrared wavelengths to search for ferrous-bearing minerals (spectral signatures near 1 μm), Fe-Ti-bearing glasses (spectral signatures near 340 nm), and ferrous iron (strong band near 250 nm). These measurements will be made with a spatial resolution of 5 km or better. Table 2 summarizes the key performance characteristics for the two channels.

Figure 3 shows the placement of MASCS on the MESSENGER spacecraft before thermal blanket installation. The instrument is mounted inside the third-stage-to-spacecraft adapter ring with its telescope optic axis aligned with the spacecraft +Z axis (Leary et al. 2007) and with the long axis of the UVVS entrance slit aligned with the spacecraft (S/C) ±Y axis. In this configuration the UVVS slit "points at" the spacecraft sunshade. Except for the telescope aperture, the entire instrument is covered with thermal blankets for flight.

4.2 Optical Design and Performance

Figure 4 is a schematic diagram of the MASCS optical system showing the major components, detectors, and telescope baffles. The design is derived from the Galileo UVS in which a Cassegrain-style, concentric-mirror telescope and a plane grating monochromator equipped with three PMT detectors form an integral optical-mechanical system. It was modified for MASCS by adding a spectrograph, which is located on an external optical bench and coupled to the telescope focal plane by an optical fiber.

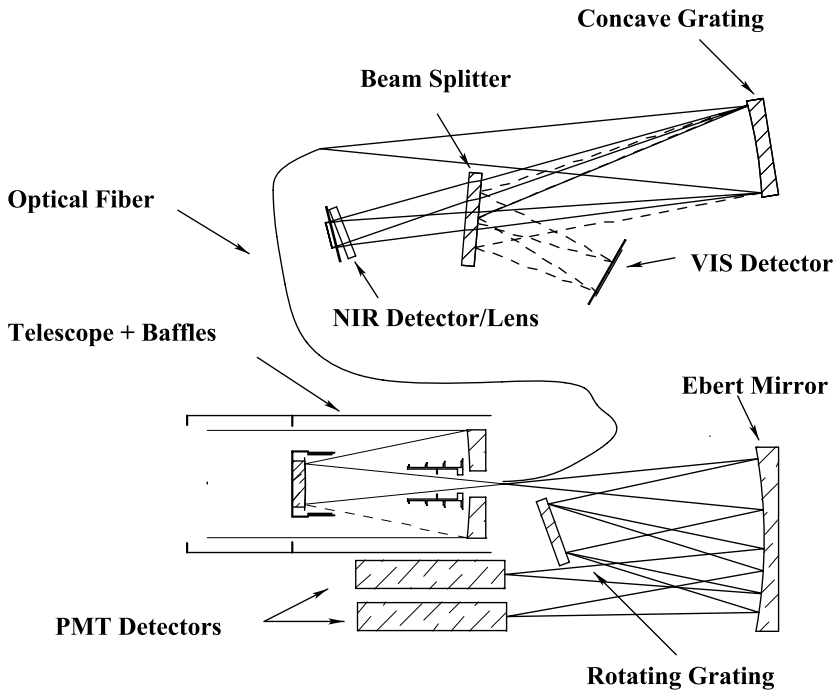#### 4.2.1 Telescope-Ultraviolet and Visible Spectrometer

The telescope optical design is a Dall-Kirkham configuration, which has a concave elliptical primary mirror with a 254.0-mm radius of curvature and a conic constant equal to 0.8786.

Table 2 MASCS instrument summary

Telescope	
Focal length	257.6 mm
Aperture	50.3 × 52.8 mm
Ultraviolet and visible spectrometer	
Focal length	125 mm
Grating	2400 groove/mm—blazed at 330 nm
Spectral resolution	
FUV channel	0.3 nm
MUV channel	0.7 nm
VIS channel	0.6 nm
Wavelength range	
FUV channel	115–190 nm
MUV channel	160–320 nm
VIS channel	250–600 nm
Field of view	
Exosphere	1° × 0.04°
Surface	0.05° × 0.04°
Visible and infrared spectrograph	
Focal length	210 mm
Grating	100 groove/mm—sinusoidal profile
Dispersion	46.6 nm/mm, 2.33 nm/pixel
Spectral resolution	4.7 nm
Wavelength range	
VIS channel	300–1,050 nm
NIR channel	850–1,450 nm
Field of view	0.023° circular
Instrument	
Mass	3.1 kg
Average power	6.7 W
Dimensions	195 × 205 × 310 mm

A convex spherical secondary mirror focuses the final image ∼17 mm behind the primary mirror vertex, producing a system with a 257.6-mm effective focal length and an $f/5$ focal ratio. Baffles located directly behind the secondary mirror and in the center of the primary mirror shield the telescope focal plane from direct illumination by the external scene.

For exosphere observations, the UVVS is equipped with a 0.175-mm-wide × 4.5-mm-long slit, corresponding to a 0.04° × 1.0° field of view (FOV). A two-position mechanism, located behind the telescope focal plane, inserts an opaque mask over the top and bottom of the exosphere slit, reducing the aperture height to 0.23 mm, to provide a 0.04° × 0.05° FOV for surface observations. The VIRS 0.023°-circular FOV is determined by the 0.1-mm diameter of the quartz optical fiber that feeds the spectrograph input. It is located 1.71 mm (0.38°) from the center of the UVVS surface slit.

Concave Grating

Beam Splitter

Optical Fiber

VIS Detector

NIR Detector/Lens

Telescope + Baffles

Ebert Mirror

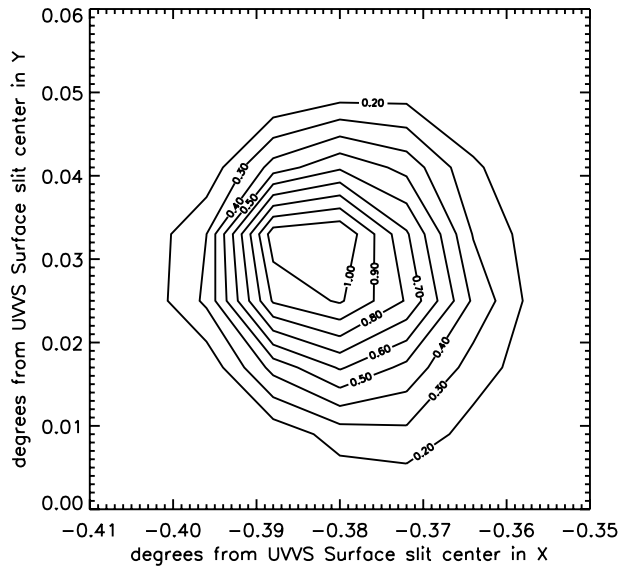**PMT Detectors**

Rotating Grating

Fig. 4 MASCS optical system schematic. For clarity, only two of the three UVVS photomultiplier tube detectors are shown

In a Dall-Kirkham telescope, spherical aberration in the primary and secondary mirrors cancel and the images near the optic axis are only blurred by coma. Spot diagrams computed from ray tracing a circular object with a 0.023° angular diameter located 100 km from the telescope aperture were used to evaluate imaging performance for the VIRS FOV. The results are shown in Fig. 5 as intensity contours, normalized to a peak value of 1. These contours represent the irradiance in the focal plane that results from convolving the telescope imaging point spread function with the angular FOV defined by the spectrograph input fiber. The shape of the contour plot is consistent with analytic estimates from third-order aberration theory, which predict that the point source comatic blur at the field location of the VIRS fiber is 8 μm compared to its 100-μm diameter. Similar results were obtained for the UVVS FOV, and the imaging performance can be accurately approximated as the convolution of an 8-μm telescope point spread function and a 0.175-mm × 4.5-mm rectangular aperture.

The UVVS spectrometer is a standard, 125-mm focal length, Ebert-Fastie design, which uses a single spherical mirror as both collimator and camera. Light from the telescope enters the spectrometer through the entrance aperture and is collimated and reflected toward the diffraction grating by one side of the Ebert mirror. After diffraction a narrow band of wavelengths is imaged onto the spectrometer focal plane by the other half of the Ebert mirror. Here three Hamamatsu photomultiplier tubes (FUV-PMT, MUV-PMT, and VIS-PMT), behind separate exit slits, each separated by 10.2 mm in the spectrometer focal plane, record the spectrum in pulse counting mode, providing maximum sensitivity for the exospheric observations. Their photocathodes (CsI for FUV, CsTe for MUV, and Bi-alkali for VIS) are chosen to optimize measurements in narrow spectral ranges and minimize the effects of

Fig. 5 Modeled imaging performance for the VIRS FOV. Contours are irradiance values normalized to 1

wavelength-dependent scattered light within the spectrometer (Hord et al. 1992). Spectral scanning is accomplished by rotating the diffraction grating in discrete steps.

Analytic calculations and ray tracing were used to select the spectrometer parameters (entrance and exit slit widths, grating spacing, and grating drive angular range and step size) required to meet the MESSENGER measurement objectives summarized in Table 1. The wavelength and imaging equations for an Ebert-Fastie spectrometer provided the point of departure for this analysis:

$$m\lambda = d\big[\sin(\alpha) + \sin(\beta)\big],$$
$$m\lambda = 2d\sin(\theta)\cos(\phi),$$
$$\theta = \frac{\beta + \alpha}{2}, \tag{1}$$
$$\phi = \frac{\beta - \alpha}{2},$$

where λ is the wavelength, d is the grating spacing, m is the diffraction order number, α is the grating angle of incidence, and β is the grating angle of diffraction. $\theta = \alpha + \phi$ is the grating rotation angle, and ϕ is the half angle difference between β and α, which is fixed by the geometry of the spectrometer and is unique for each channel. Rotating the grating through angle $\Delta\theta_S$ changes the wavelength by $\Delta\lambda_S$ given by

$$\Delta\lambda_S = \frac{2d\cos(\theta)\cos(\phi)}{m}\Delta\theta_S. \tag{2}$$

The minimum step size consistent with minimum Nyquist sampling is 1/2-bandpass-per-step. A goal for the MASCS design was to reduce that step size by 33%, providing about three steps per bandpass.

The UVVS imaging function for a monochromatic line is the convolution of the image of the entrance slit with the physical width w_{en} of the exit slit. In the absence of image

aberration, the entrance slit image width is given by:

$$w'_{en} = w_{en} \cdot \cos(\alpha) / \cos(\beta). \tag{3}$$

The ratio of cosines is referred to as anamorphic magnification.

For an Ebert-Fastie configuration, the image of the entrance slit is always larger than the slit itself, and the resulting imaging function is a trapezoid with a full-width half maximum (FWHM) equal to the greater of the entrance slit image or the exit slit width. Differentiating the standard grating equation with respect to the diffraction angle, β, and multiplying by the angular width of the imaging function gives an expression for the spectrometer bandpass

$$\Delta\lambda = \frac{d}{m \cdot F_l} \cdot \cos(\beta) \cdot w_{ex} \quad \text{when } \cos(\beta) \cdot w_{ex} > \cos(\alpha) \cdot w_{en},$$

$$\Delta\lambda = \frac{d}{m \cdot F_l} \cdot \cos(\alpha) \cdot w_{en} \quad \text{when } \cos(\alpha) \cdot w_{en} > \cos(\beta) \cdot w_{ex}, \tag{4}$$

where $F_l = 125$ mm is the spectrometer focal length and w_{en} and w_{ex} are the entrance and exit slit widths, respectively. If the spectrometer imaging aberration is negligible, then the instrument spectral resolution is equal to the bandpass. Equation (4) shows that for fixed bandpass, smaller values of grating spacing lead to wider slits and therefore greater instrument sensitivity (see (6) in Sect. 5). An assumed maximum grating rotation angle of $\sim 45°$ limits the smallest spacing from commercially available gratings to 416.67 nm (2,400 grooves mm^{-1}).

In order to maintain high efficiency, it is common practice to restrict the operating wavelengths for a diffraction grating to a range specified by the blaze wavelength, λ_B: $2\lambda_B/3 < \lambda < 2\lambda_B$ (James and Sternberg 1969). The blaze wavelength is related to the blaze angle, which is the angle that the groove facets make with respect to the grating normal, through (1) when $\phi = 0$ [$\lambda_B = 2d\sin(\theta_B)$]. A 600-nm maximum operating wavelength suggests $\lambda_B \geq 300$ nm and a 200-nm minimum operating wavelength. Since the blaze range is actually a restriction on incidence and diffraction angles, high efficiency for the FUV wavelength range is accommodated in MASCS by using the grating in second order ($m = 2$), resulting in an effective first-order range 230–380 nm. These considerations led to the selection of a standard catalog Jobin Yvon grating with a 2,400-g/mm ruling density and a 330-nm blaze wavelength for the UVVS.

Once the grating was selected, ray-tracing trade studies were used to maximize entrance and exit slit widths and to place the VIS detector in the focal plane, consistent with the requirement that the instrument resolve the sodium resonance doublet, i.e., the D1 and D2 lines. Although (4) suggests that placing the VIS detector at the outboard position in the focal plane to maximize β will produce the best spectral resolution, the strong variation in instrument point spread function across the focal plane causes the inboard position to be the best choice of the three. The values selected from the trade study for entrance and exit slits are 0.175 mm and 0.23 mm, respectively. Spectral bandpasses using these slits and a 2,400-g/mm grating are shown in Fig. 6 as solid lines. Dashed curves show the spectral sampling for the three channels obtained with a 1-arcmin grating step size ($\Delta\theta_S = 0.0167°$), providing the required $\sim 1/3$ bandpass interval.

The adopted UVVS design meets its requirement to resolve the sodium doublet over the entire range of permissible D1/D2 emission ratios. This is demonstrated by the two ray-tracing model profiles shown in Fig. 7 constructed for the limiting cases where the column
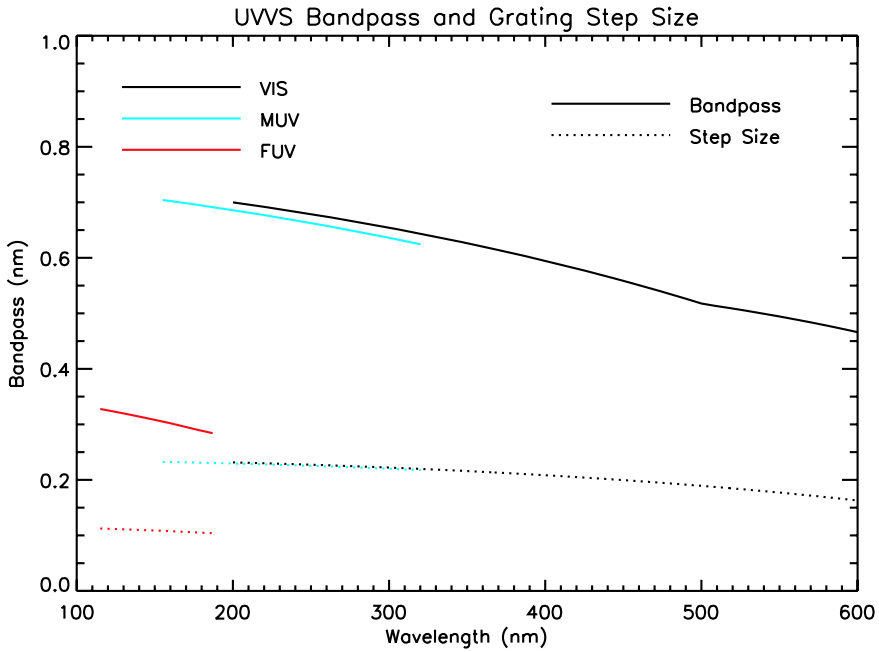
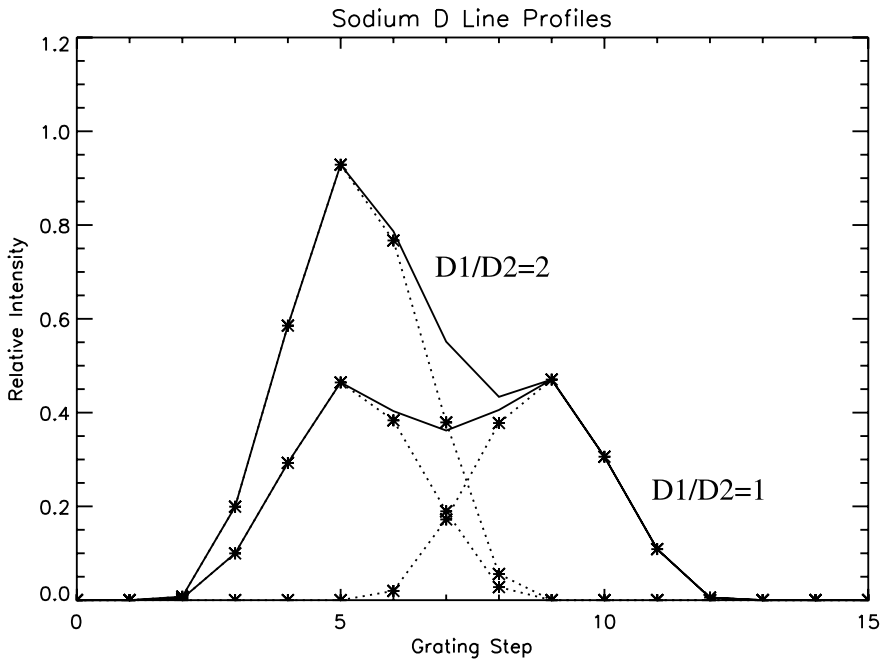**Fig. 6** UVVS channel bandpasses and spectral sampling intervals

Fig. 7 Ray-trace models for UVVS observations of the sodium D lines in the two limiting cases D1/D2 = 1 and D1/D2 = 2. *Solid curves* show the observed profiles, which are the sum of the individual emission lines (*dotted lines*). *Stars* mark the "observed values" at the individual grating positions

emission in both lines is optically thick (D1/D2 = 1) and optically thin (D1/D2 = 2). Al-though the spectrometer point spread function causes the spectral resolution to be approxi-mately 15% larger than the bandpass shown in Fig. 6, the two emission lines are separable in both cases. Additional ray-tracing analysis demonstrated that this resolution performance is maintained over the entire operating temperature range of the instrument ($-30°C$ to $+30°C$).

4.2.2 Visible and Near-Infrared Spectrograph

A single-mode optical fiber, which InnovaQuartz, Inc., of Phoenix, AZ, contributed to the MASCS project, transmits light from the telescope focal plane to the VIRS spectrograph. It was fabricated from fused silica with low water content, which minimizes the light loss caused by strong OH absorption at 1.2 μ that is often encountered in commercial fibers, and was drawn to maintain an $f/5$ beam divergence compatible with the telescope. The polished output surface of the fiber, which is 100 μm in diameter, provides the entrance aperture to the spectrograph.

The VIRS uses a concave grating to both disperse and image the spectrum onto an ex-tended focal plane. Light diverges from the fiber output and is diffracted and imaged by the grating toward a beam splitter, which reflects visible wavelengths onto a silicon (Si) pho-todiode array detector, referred to as the VIS detector. Infrared wavelengths are transmitted by the beam splitter and are imaged onto an array of indium-gallium-arsenide (InGaAs) photodiodes, after passing through a condensing lens located directly in front of the NIR detector.

In addition to meeting the measurement requirements for spectral coverage (300–1,450 nm) and spectral resolution (5 nm), the VIRS optical design was constrained to use ex-isting, commercially available detectors and grating and to fit within the UVVS mechanical footprint. MASCS uses self-scanning array detectors, developed by Hamamatsu Corpora-tion, to record simultaneously the visible (300–1,050 nm) and near-infrared (880–1,450 nm) spectrum. Hamamatsu produces Si arrays in a variety of formats up to 512 in length with pixel dimensions that are either 50-μm wide × 500-μm tall or 50-μm wide × 2,500-μm tall. InGaAs pixels are restricted to a single length, which is 500-μm tall. A 50-μm pixel pitch is well matched to the input fiber diameter, satisfying the standard minimum Nyquist sampling requirement (two pixels per resolution element). If two pixels span a 5-nm spectral resolu-tion element over a 100-μm displacement in the focal plane, then the grating has to provide 50-nm-per-mm dispersion. This had to fit within an instrument with an overall length of 250 mm, which limited the VIRS grating focal length to ~200 mm. The dispersion equation for a fixed grating spectrograph defines the relationship between ruling density and focal length

$$\frac{d\lambda}{dx} = \frac{d\cos(\beta)}{m \cdot F}, \tag{5}$$

where $d\lambda/dx$ is the linear dispersion at the focal plane and F is the spectrograph focal length. If $d\lambda/dx = 50$ nm per mm and $F \sim 200$ mm, then $d \sim 10^4$ nm, assuming β is small. Only a small number of off-the-shelf gratings exist that have parameters close to those required for VIRS. Of these, the Jobin Yvon grating 523-00-060 provides the best match for the VIRS application. This grating is concave with a 210.6-mm radius of curva-ture and an average of 100-grooves-per-mm ruling density, providing a nominal dispersion of 46.6 nm per mm (2.33 nm per 50-μm pixel). It is manufactured using holographic record-ing as a Type II grating that produces a flat focal plane and good spectral imaging over the entire 250–1450 nm wavelength range with a point spread function that has a 10-μm or

less FWHM. In the cross-dispersion direction the output image height for the 0.1 mm entrance fiber grows to as much as 1.5 mm at the shortest wavelengths in the VIRS spectrum (near 300 nm) and up to 0.75 mm at the longest wavelengths (near 1,450 nm) because the 523-00-060 is corrected for astigmatism at only a single wavelength (1,050 nm).
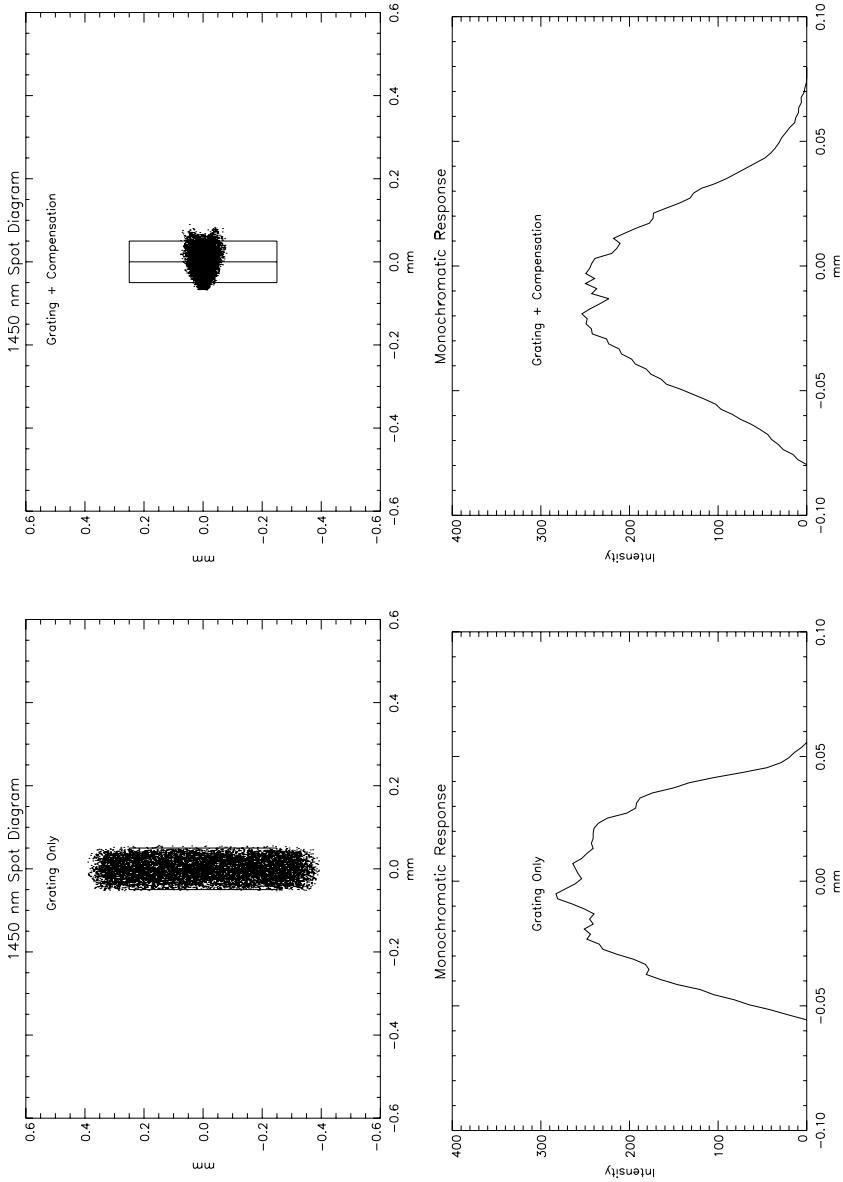
The VIS detector pixels are tall enough to accommodate the astigmatic images produced by the grating. On the other hand, fore optics are required to compress the spectrum in the cross-dispersion direction before it is imaged onto the NIR array. This is accomplished by fabricating a beam splitter with a cylindrical second surface and placing a fused silica cylindrical, convex-plano lens directly in front of the array. The beam splitter second surface, which has a 250-mm radius of curvature, causes the rays from the grating to focus behind the detector in the vertical dimension. They are subsequently compressed by the condensing lens, which has a 6.6-mm radius on its first surface, and reimaged on the detector with an average demagnification of 2. Because the magnitude of astigmatism introduced by the grating changes with wavelength, the lens must be tilted to increase the degree of demagnification toward longer wavelengths. Figure 8 compares the imaging performance for the two configurations at $\lambda = 1,450$ nm.

The left column shows a spot diagram and intensity profile for the grating and a 6.2-mm-thick beam splitter with plane-parallel faces. The right column shows the corresponding plots for the VIRS flight design, which includes a 6.1-mm-thick beam splitter with plano-concave surfaces and the tilted condensing lens. Although adding the condensing lens slightly degrades spectral imaging performance (shown in the lower two panels), the design still exceeds the 5-nm performance requirement.
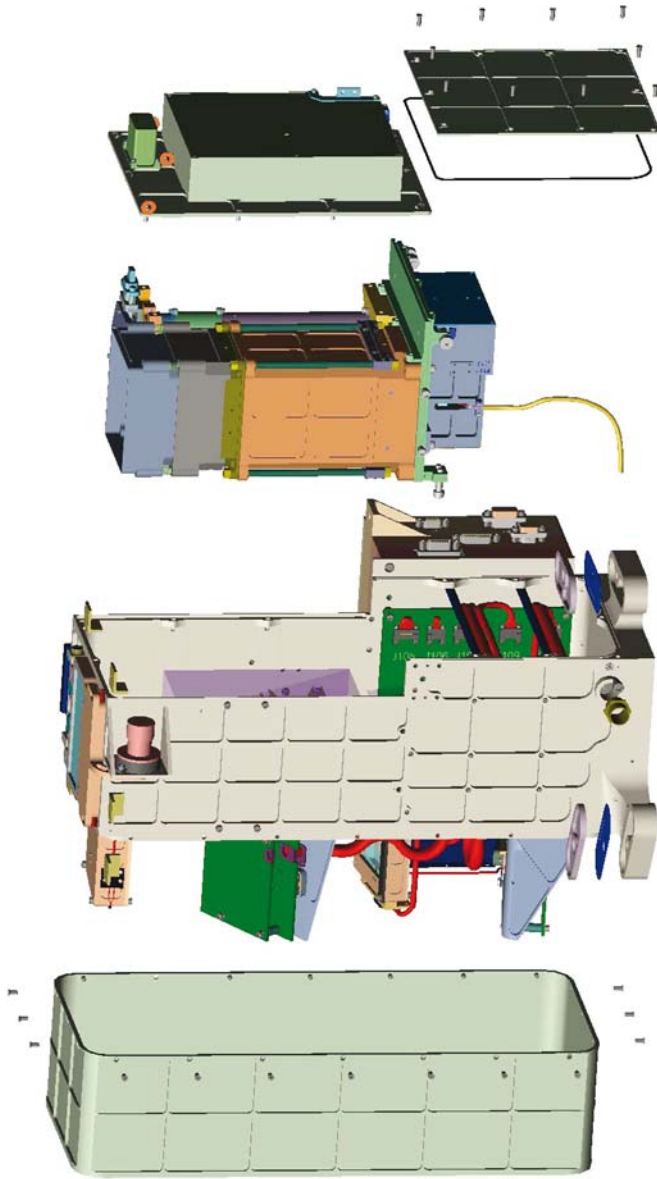
Once the imaging performance is determined from ray tracing, the detector array coverage and beam splitter coatings can be defined. At a 50-μm pitch approximately 365 pixels of the VIS array are required to capture the spectral range 200–1,050 nm. (This somewhat broader range provided additional pixels below and above the nominal instrument sensitivity cutoff, which can be used to measure backgrounds and scattered light.) For wavelengths greater than 550 nm (pixels greater than 153), the detector input window was coated with a long-wavelength-pass filter to suppress contamination of the spectral signal by short-wavelength light diffracted into second order by the grating (Maymon et al. 1988). Wavelengths 895–1,490 nm cover the 256 pixels of the NIR array. No order-sorting filter is required for NIR because InGaAS photodiode sensitivity has a short-wavelength cutoff at 750 nm. The initial beam splitter concept employed a multilayer dichroic coating for its first surface and an infrared antireflection coating for its output surface. This design was later abandoned for the flight instrument in favor of a more robust approach in which the top half of the first surface was coated with Al and its bottom half with an infrared antireflection coating.

4.3 Design Approach

An exploded view of MASCS is shown in Fig. 9. Its design was strongly driven by the MESSENGER mission mass constraints. As originally proposed, MASCS was intended to follow closely the mechanical design of the Galileo UVS with additional structure to support the VIRS optical elements and detectors. The MASCS UVVS section is optically very similar to the Galileo UVS, and since the VIRS section is coupled to the UVVS telescope by a flexible fiber optic its location was not critical as long as its elements were correctly located in relation to each other. However, a detailed study showed that a one-piece instrument case could result in a lighter instrument than the assembly-of-boxes heritage design from the Galileo UVS.

Fig. 8 Imaging performance comparison at $\lambda = 1,450$ nm. The *left* and *right* columns show spot diagrams and intensity profiles for the grating + plane-parallel beam splitter and for the grating + beam splitter + condensing lens, respectively. In both cases the spectrograph input is the 100-μm diameter fiber aperture. The condensing lens is required to match the spectral image to the size of an NIR detector pixel pair (*solid lines* in the *upper panels*), which defines a spectral resolution element for the spectrograph

Fig. 9 An exploded view of MASCS. The *right side* of the figure shows the two major assemblies that comprise the UVVS component. The *left side* shows the VIRS cover

The case provides five sides of the UVVS enclosure. The back face of the case serves as an optical bench for the VIRS section of the instrument. The VIRS components are completely accessible by removal of a cover. The fiber optic input and shutter mount, grating, beamsplitter, and both detectors could be adjusted during alignment without disturbing other parts of the instrument.

The UVVS assembly mounts inside the case and is designed so that it can be removed as a unit. With the exception of the Ebert mirror, which is mounted in the base of the instrument case, all UVVS components are mounted to an optical bench that is perpendicular to the optic axis. The optical bench is located at the plane of the spectrometer entrance and exit slits, so the telescope and PMT assembly are mounted on one face while the grating drive is mounted on the other. The optical bench maintains repeatable alignment with the instrument case with a combination of dowel pins and precision shoulder screws. The high-voltage power supply is mounted directly above the PMT assembly. The base of the high-voltage power supply enclosure acts as a lid to close out the forward portion of the instrument case. A separate cover seals the rear portion of the case. All cover joints have machined channels and small-diameter O-ring seals to prevent light leaks.

The UVVS Ebert mirror is mounted in a cell machined into the base of the case. As with most other MASCS optical elements, hard pads and opposing springs secure the mirror against launch vibration loads while allowing adjustments during spectrometer alignment.

A hinged cover over the telescope aperture protects the optics from external contamination. The cover is a spring-loaded, one-time release mechanism that is opened in flight after spacecraft outgassing has reached an acceptable level. The cover is manually reclosable for ground operations. A $MgFl_2$ window in the cover exposes half of the telescope aperture to facilitate ground testing and to ensure that a cover failure cannot prevent MASCS from accomplishing its science goals. In the closed position the cover is held in place by a pin-in-hole latch. When the pin is retracted, redundant torsion springs open the cover, rotating it by 190° about the hinge. The pin is part of a TiNi Aerospace pinpuller mounted on the instrument case. The pin is held in the extended position by an internal shape memory alloy (SMA) latch. To actuate the pinpuller MASCS applies power to either of a pair of redundant heaters in the device, releasing the SMA latch. An internal spring then retracts the pin, allowing the cover to open.

The base of the case includes the three integral flexure-mounting feet that mount the instrument to the spacecraft deck (Leary et al. 2007). The flexure design mitigates the coefficient of thermal expansion mismatch between the magnesium case and the composite deck. A titanium cap plate over each foot adds stiffness against launch vibration loads while allowing the feet to flex radially. The feet are 120° apart and are designed so the instrument boresight does not move relative to the deck as a result of temperature variations. Titanium washers are installed under each foot to minimize heat transfer between MASCS and the instrument deck. MASCS is bolted directly to its mounting points in the deck; no shimming was required to meet alignment requirements.

The instrument case and most other structural pieces are machined from magnesium and aggressively weight-relieved. Some small parts are machined from aluminum where the difference in mass compared to magnesium is small. The magnesium parts are electroless nickel plated for corrosion resistance and conductivity. Black paint is applied over much of the case surface to enhance optical and thermal properties. The extensive use of magnesium reduced the mass of the instrument significantly, though the cost of manufacturing the parts was somewhat higher than it would have been for an all-aluminum structure. Overall, the use of magnesium saved approximately 0.4 kg, a significant savings in a 3.1-kg instrument.

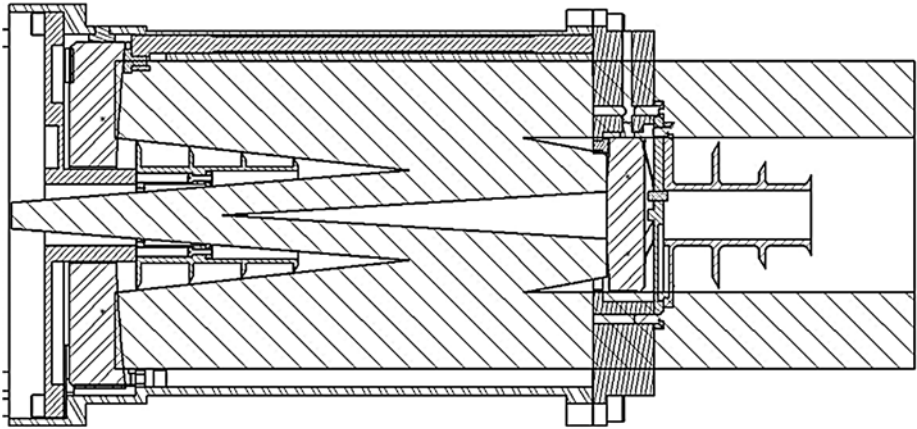**Fig. 10** Solid-model drawing showing the UVVS components

4.4 Telescope-Ultraviolet and Visible Spectrometer

Figure 10 is a solid-model drawing that shows the details of the Telescope-Ultraviolet and Visible Spectrometer mechanical assembly and its five major components: telescope, entrance aperture plate, grating drive, detector head, and Ebert mirror. Four of these components mount directly to a central plate that is oriented perpendicular to the optic axis. In this drawing two instrument covers, as well as a telescoping light shield between the front of the telescope housing and the door on the front of the instrument case, are not shown.

4.4.1 Telescope

Figure 11 shows a cross-section view of the MASCS telescope, which was adapted from the Galileo UVS telescope design with only minor modification. In this design, the telescope housing, which attaches directly to the central mounting plate with screws and locating pins, acts as the primary structural element. The primary mirror is registered in the housing laterally by Cu–Be leaf springs that push the mirror against Vespel® side pads. A back plate with a central hub, which contains the mounting surface for the telescope central baffle, and additional leaf springs register the optical surface of the primary against gold-alloy pads inserted into the housing. The secondary is retained by springs and pads located in a separate mirror cell that is attached to the ends of three invar metering rods, rather than to the main housing. The other end of each rod is attached to the telescope housing near the location of the primary mirror optical surface. As the aluminum housing expands and contracts with changes in temperature, the invar rods, which have a thermal expansion coefficient that is matched to that of the fused silica mirrors, maintain a nearly fixed primary-to-secondary separation. This allows the telescope to image over the instrument operational temperature range without significant change in focus.

The MASCS metering system is an improvement over the Galileo design in which the secondary cell was mounted to the telescope housing and invar rods contacted the primary

Fig. 11 Telescope cross-section view

mirror optical surface. In that configuration the primary-to-secondary distance was maintained, but both mirrors were free to move relative to the telescope focal plane, causing a small shift in focus. This was acceptable for Galileo because it operated over a much smaller temperature range than MASCS will encounter in Mercury orbit.
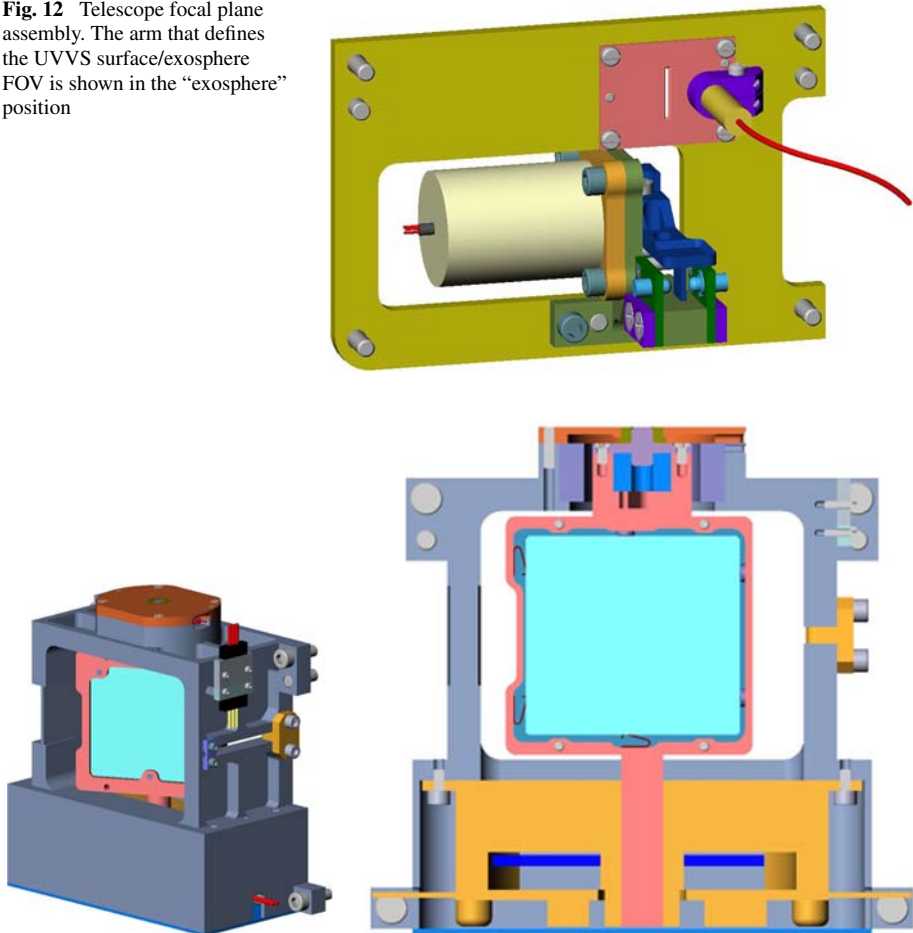
Suppression of stray and scattered light within the MASCS telescope is important because the instrument must observe faint exospheric emissions above the sunlit limb of Mercury. Primary and secondary mirror baffles shield the telescope focal plane from direct illumination by the external scene. The primary baffle was fabricated as a series of concentric rings to minimize grazing incidence reflections from its exterior. In addition, the walls of the main housing are coated with black anodizing, and the primary and secondary baffles are plated with black-nickel to suppress secondary light scattering from those surfaces. Finally a light shield is installed between the front of the telescope housing and the instrument door to seal the telescope cavity against leaks.

4.4.2 Telescope Focal Plane Assembly

Light from the telescope is focused onto an aperture plate assembly, which holds both the UVVS entrance slit and the VIRS input fiber. Figure 12 shows a view of this assembly as seen from inside the spectrometer. The UVVS slit, which is 4.4 mm long × 0.175 mm wide, is photoetched into a 1.3-mm-thick nickel substrate and is located on the main assembly plate with steel dowel pins. A ferrule that holds the fiber optic feed for the VIRS is mounted next to the UVVS slit.

The aperture plate also supports the mechanism that selects either the exosphere or surface FOV for the UVVS. For the surface mode, an Aeroflex 16305 stepper motor, which has a 10-mm diameter, rotates a balanced arm counter clockwise through 90° in order to cover the UVVS slit. This places a 0.22-mm-wide horizontal slot across the center of the slit defining a 0.04°-wide by 0.05°-tall field-of-view. For exosphere mode the motor rotates the arm clockwise to the position shown in Fig. 12. In this orientation, a small knife edge located on the back of the arm breaks the light path between a light emitting and receiving diode pair, producing an electrical signal that indicates its location.

Fig. 12 Telescope focal plane assembly. The arm that defines the UVVS surface/exosphere FOV is shown in the "exosphere" position
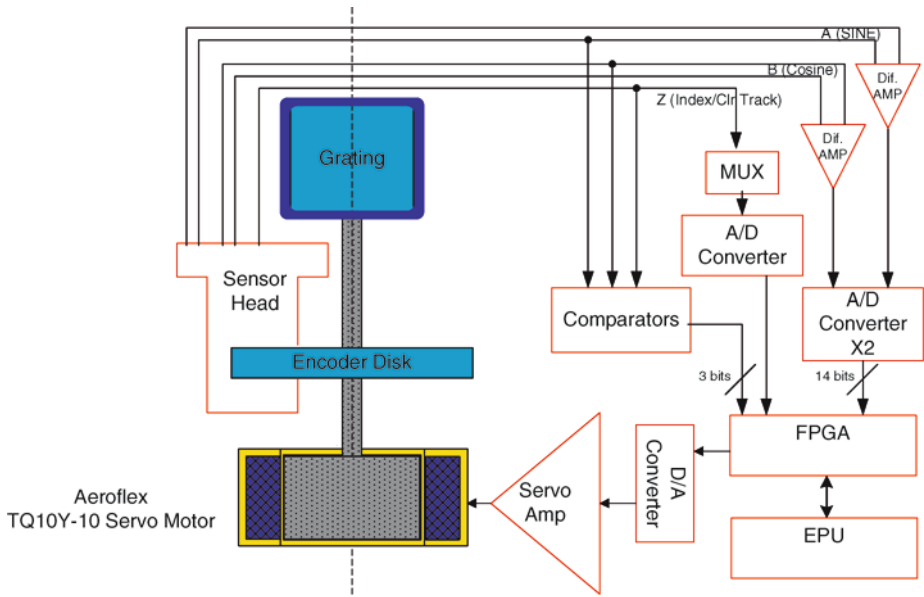

Fig. 13 Solid-model and cut-away views of the UVVS grating drive mechanical assembly

4.4.3 Grating Drive Assembly

The UVVS incorporates a grating drive assembly that provides the required precise rotation of the spectrometer grating. The full range of the grating rotation is limited by hard stops to approximately 45°, with a minimum step size of 1 arcmin. The required accuracy is ±15 arcsec, with a settling time of 1 ms per step. The maximum rate of the grating drive is 200 steps per second. The grating drive assembly, which is shown in Fig. 13, consists of a magnesium housing supporting a grating rotor, drive motor, and optical position encoder. The grating drive assembly is removable from the instrument as a unit for ease of testing.

The grating rotor is a single machined part that supports the grating and provides concentric shafts at opposite ends for the drive motor and the position encoder. The grating itself is approximately 33-mm wide by 30-mm tall. It is mounted in the rotor with adjustable hard pads that allow alignment in tip, tilt, and focus. Opposing springs ensure that the grating is firmly located against the hard pads. The drive motor is a brushless DC torque motor procured from Aeroflex.

Fig. 14 UVVS grating drive control system block diagram. MUX denotes a mutiplexer

The optical encoder is a semi-custom unit procured from Dynamics Research Corporation. The design uses a rotating glass encoder disk and fixed reticules with light-emitting-diode (LED)/phototransistor pairs to generate and sense fringe patterns. The encoder glass produces 4,096 cycles per full revolution. This allows coarse position knowledge to about 5-arcmin resolution. The LED/phototransistor pairs produce two sinusoidal signals (A and B) 90° out of phase. Interpolation by a factor of 32 allows fine position knowledge at better than 10-arcsec resolution, which is sufficient for the grating drive control system to meet the rotational position requirement. A separate index track on the encoder disk provides a zero reference point. Since most of the index track is clear, the index signal is also used to monitor signal level degradation over the life of the mission. The encoder indicates relative rather than absolute rotation, so the zero reference index must be found after each power cycle.

Figure 14 shows the block diagram for the grating drive position closed-loop control system, which is implemented in a combination of hardware and software. Encoder signals are processed in a field-programmable gate array (FPGA) on the Digital Electronics Board (DEB, see Sect. 4.5).

The grating drive is initialized by a two-step process when the instrument is powered on. The first step generates a look-up table that is used for efficient position calculations. Software, which is resident within the instrument Event Processing Unit (EPU), commands the drive motor to sweep from one hard stop to the other in an open-loop mode and monitors the A and B encoder signals to establish their full dynamic range, then calculates and stores in memory the interpolated arctan look-up table that allows quick position determination within an encoder cycle. Since the table is calculated using the measured dynamic range of the encoder signals, small variations over the life of the mission are compensated automatically. Larger variations can be compensated by changing the power levels of the LEDs by software command. Lookup table generation takes about 20 s to complete.

The second step in grating drive initialization finds the index mark of the encoder and establishes the zero reference position. This zero reference position is near the center of travel. It is used internally by the software as an offset so that from the user's point of view all commanded grating step positions are positive, with step 0 near the short-wavelength hard stop.
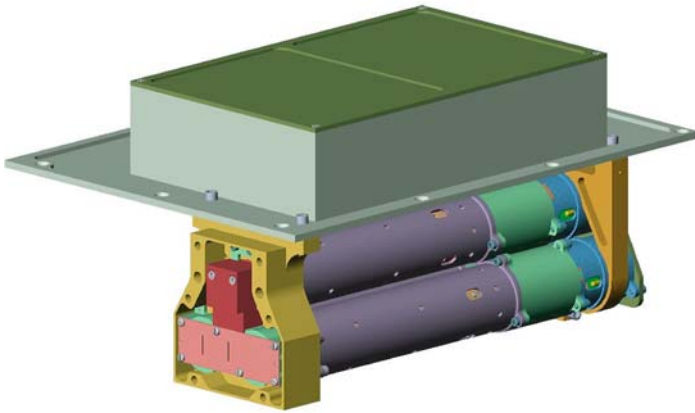
The position control algorithm is a proportional-integral-differential (PID) calculation with an added feed-forward element to improve step performance. The control loop runs at 3 kHz. A hardware timer in the FPGA on the DEB generates a 3-kHz interrupt to the microprocessor. The FPGA also controls the output signals to the drive motor and the input signals from the encoder at 3 kHz, providing precise timing for the control loop. The FPGA also maintains a coarse position counter by monitoring and comparing the encoder A and B signals. This hardware "fringe counter" ensures that the control system has positive knowledge of each encoder cycle and relaxes software real-time performance requirements.

At each 3-kHz interrupt the software calculates the current position by reading FPGA registers to retrieve the latest values of the A and B signals, then uses those values as indices into the look-up table to determine the position within the current encoder cycle. This position is added to the coarse position counter value, also retrieved from an FPGA register, to give the current position. The current position is compared with the desired position to derive the position error, which becomes the input to the PID calculation. The output of that calculation is written to an FPGA register. At the start of the next control cycle the FPGA writes this value to the digital-to-analog (D/A) converter that controls the grating drive motor current to reposition the grating. The feed-forward parameter of the control system takes effect when the commanded step position changes. It provides an additional boost to the drive motor during the first three control cycles of a step to maximize the initial acceleration of the mechanism without affecting the stability of the PID control when the grating settles at the new position.

In operation the UVVS scans a wavelength region of interest by stepping the grating so that a series of discrete wavelengths are presented to the spectrometer exit slits and thus to the PMTs. Commonly commanded modes include short back-and-forth or "zigzag" scans across a spectral feature and longer one-direction scans to explore a wider spectral range. At each point of the scan the grating drive steps to the next desired position, then accumulates data from one or two of the three photomultiplier tubes for the commanded integration time. At the end of each integration time the grating drive moves to the next position until the commanded scan is complete. The step size is commandable from 0 to 15 arcmin in 1-arcmin steps. If the step size is 0 the grating drive controls at a single position and the integrations are performed back to back.

Two commandable parameters help ensure that the grating position will be stable during the integration times. First, the time allowed for the grating drive to step and settle is configurable in units of 1/3,000 s. Second, the timing between the end of an integration period and the start of the next step can be modified so that the step begins just before the integration time ends. This phase offset parameter takes advantage of the fact that the grating does not actually move out of the position tolerance band for a step at the instant the step is initiated.

Grating drive health and performance are monitored in flight. Each UVVS science telemetry packet includes a counter value indicating the number of control cycles in which the grating drive position exceeded its ± 15 arcsec tolerance band. This provides a measure of performance during each UVVS observation. The grating drive can also be commanded to perform a step response test during which a configurable set of control system parameters are sampled at 3 kHz. This test generates diagnostic telemetry packets, which are downlinked and analyzed to determine grating drive step performance.

Fig. 15 Detector head assembly

4.4.4 UVVS Detector Assembly

The instrument detector head assembly is shown in Fig. 15. It consists of a pair of tri-brackets that support the three individual photomultiplier tube assemblies and the spectrometer exit slit assembly.

Each exit slit pair is separated by 10.2 mm. This spacing, which is smaller than the 13.5-mm diameter of an individual tube, is accommodated by placing the MUV detector above the spectrometer dispersion plane. A pair of mirrors that are oriented at 45° with respect to the light path form a periscope, which directs light from the middle exit slit to the tube (see Fig. 16). Spherical surfaces on the mirrors funnel the diverging beam toward the center of the detector input window. The bottom of the high-voltage power supply (HVPS) housing, which is oversized to form a cover for the detector assembly after it is mounted in the main instrument case (see Fig. 9), provides lateral support for the tri-brackets. High-voltage connections to the detectors are hard-wired to feed-through connectors that protrude through the bottom of the HVPS. External electrical connections to the detector assembly are made through a single 25-pin Airborn micro-connector. This design allows the entire assembly to be easily removed from the instrument without disturbing the sensitive high-voltage connections, which are encapsulated for flight.
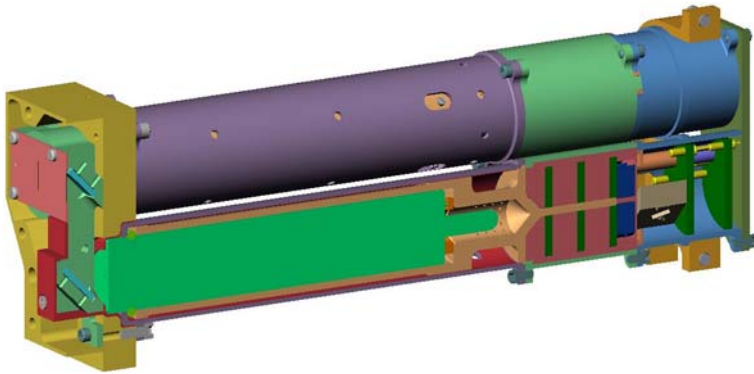
Hamamatsu photomultipliers, from the 13-mm diameter head-on family, were selected for MASCS, replacing the EMR Photoelectric 510-series detectors used in the Galileo UVS. The UVVS detectors operate in pulse-counting mode with grounded photocathodes and output pulses capacitively coupled into Amptek A-111F pulse-amplifier-discriminators (PADs). A-111F PADs are high-sensitivity ($\sim 5 \times 10^4$ e$^-$), hybrid devices with a $\sim$500-ns pulse-pair resolution.

Although the Hamamatsu tubes' borosilicate glass envelopes make them less rugged than 510 detectors, their larger active areas significantly increase the instrument FOV uniformity. Their multiplication sections have ten-stage linear-focused dynodes, which produce stable, saturated pulse height distributions. Multiplier modal gain is photocathode dependent. Table 3 summarizes the operating characteristics for three UVVS wavelength ranges.

The detectors were subjected to a comprehensive characterization and qualification program because only the R1081 had been previously used for a long-duration spaceflight application (Esposito et al. 2004). Characterization measurements for all tubes included quantum

Table 3 UVVS detector characteristics

Parameter	Value		
	FUV channel	MUV channel	VIS channel
Type number	R1081	R759	R760P
Photocathode	CsI	CsTe	BiAlkali
Window material	MgF$_2$	Fused silica	Fused silica
Dynode material	BeCu	Cs$_3$Sb	Cs$_3$Sb
Operating voltage	1,800–2,250 V	800–1,250 V	800–1,250 V
Modal gain	1×10^6	2×10^6	3×10^6
Photocathode diameter	6 mm	10 mm	10 mm

Fig. 16 UVVS photomultiplier tube assembly cross-section view

efficiency, photocathode spatial uniformity, and pulse height distribution, measured as functions of accumulated counts ranging from an initial value of 10^8 to a final value of 10^{10}. No degradation in the modal gain was detected for this level of accumulated count. There was no detectable loss in responsivity with amplifier thresholds set at flight values (1×10^5 e$^-$ for CsTe, 5×10^4 e$^-$ for CsI, and 1×10^5 e$^-$ for BiAlkali), and no detectable change in spatial uniformity. Just before final assembly, the operating voltage for each tube was determined by illuminating it with a constant-intensity light source and identifying the plateau in a plot of output count versus high voltage.

Figure 16 shows a cut-away drawing with a cross-section view of the MUV detector and the periscope assembly. The 13.5-mm-diameter × 71-mm-long tube is registered inside a Delrin sleeve by an O-ring at the front and a slip fit at the rear. Twelve feed-through pins, which provide the electrical connections to the dynodes and photocathode, exit the detector at the rear.

A 13-mm-diameter three-board circuit stack, which provides the resistor divider chain for the high voltage, is soldered directly to dynode pins. The entire area around the output pins and divider circuit is encapsulated to provide mechanical rigidity and protection from high-voltage arcing. Two additional 13-mm diameter boards carry the A-111F amplifier and its output-pulse driver electronics. A μ-metal housing with a 10-mm-diameter aperture, located 5 mm in front of the input window, surrounds the entire photomultiplier tube to protect it from magnetic fields. Laboratory tests show that this shield geometry is adequate

to eliminate magnetic field effects for strengths at the detector of up to 15 gauss, which is a factor of 5 greater than ambient fields produced by torque motors, located in the exit slit housing ($\sim$2.5 gauss at the tube).
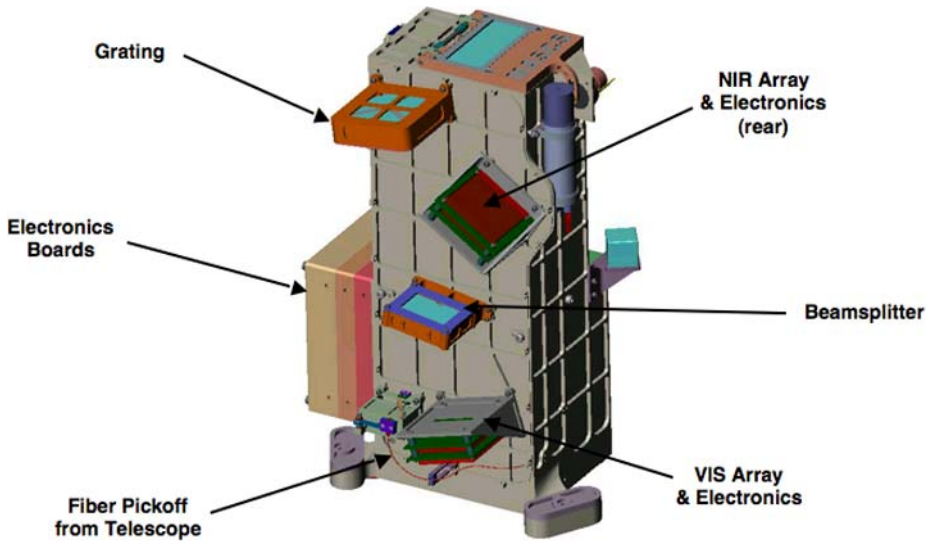
Two effects cause the UVVS detector outputs to exhibit a small but nonnegligible dependence on temperature. The smaller of the two arises from small variations in the high-voltage power supply output and divider string resistance, which cause the multiplier gain to fluctuate with temperature. For the UVVS detectors, the measured value for the relative change in output is $\sim 5 \times 10^{-5}$/°C. The larger of the two arises from the fact that the quantum efficiencies of all photocathodes are temperature dependent. Temperature coefficients depend upon both photocathode material and the wavelength of the incoming light. The relative changes for the UVVS detectors can be as large as 0.008/°C for CsTe and BiAlkali at the longest observed wavelengths. Accurate preflight calibrations and in-flight measurements of detector head temperature allow these effects to be corrected to $\sim$2%.

A single HVPS, equipped with three Amptek HV601 high-voltage opto-isolators, provides 2,040, 900, and 900 V to the FUV, MUV, and VIS tubes, respectively. The primary supply, which operates at a nominal 2,250 V, uses a 50-kHz oscillator to drive a six-stage Cockroft-Walton voltage multiplier to produce unregulated high voltage for the 601s. Custom-regulated high voltage for each tube is produced by using a 601 in a closed-loop control system that compares output voltage, which has been divided by 10^3, to a fixed reference voltage, which was determined from that detector's output count versus high-voltage plot. The entire supply is mounted on three printed circuit boards and enclosed in a magnesium housing, which measures $7.0 \times 11.1 \times 2.5$ cm. Its mass, after encapsulation, is 250 g and its nominal operating power, referenced to its input, is 370 mW with all three detectors operating. Flight operations limit the maximum number of operating tubes to two, for which the output power is 320 mW. Bench tests, performed before instrument assembly, showed that the high-voltage output was stable to $\pm$10 V over an operating temperature range from -45°C to $+45$°C.

4.5 Visible and Near Infrared Spectrograph

Figure 17 is a solid-model drawing that shows the details of the Visible and Near Infrared Spectrograph mechanical assembly and its five major components: entrance aperture assembly, grating, beam splitter, and two detector heads. Unlike the majority of the UVVS components, which are tightly integrated into a single mechanical package, the VIRS assemblies mount in individual holders that attach to an optical bench, which is one surface of the MASCS instrument case. Pairs of dowel pins pressed into each optical mount allow for easy removal and replacement of elements without the loss of precise optical alignment. The optical elements themselves are mounted in cells that use leaf springs and pads to locate their optical surfaces except for a condensing lens, which is bonded into a mounting flange that attaches to the front of the NIR detector housing. A lightweight cover, which is sealed by an O-ring that is captured in the optical bench to enclose the spectrograph, is not shown.

Stray and scattered light within the spectrograph is suppressed using surface treatments and by masking all unused surface area on both grating and beam splitter. Exterior surfaces of all the component holders are coated with black anodizing. The bench and cover interior are covered with a black polyimide-based paint. Finally, a light baffle, which is not shown in the figure, is mounted between the inboard side of the entrance assembly and the beam splitter to shield the detectors from direct illumination by light from the spectrograph input fiber.
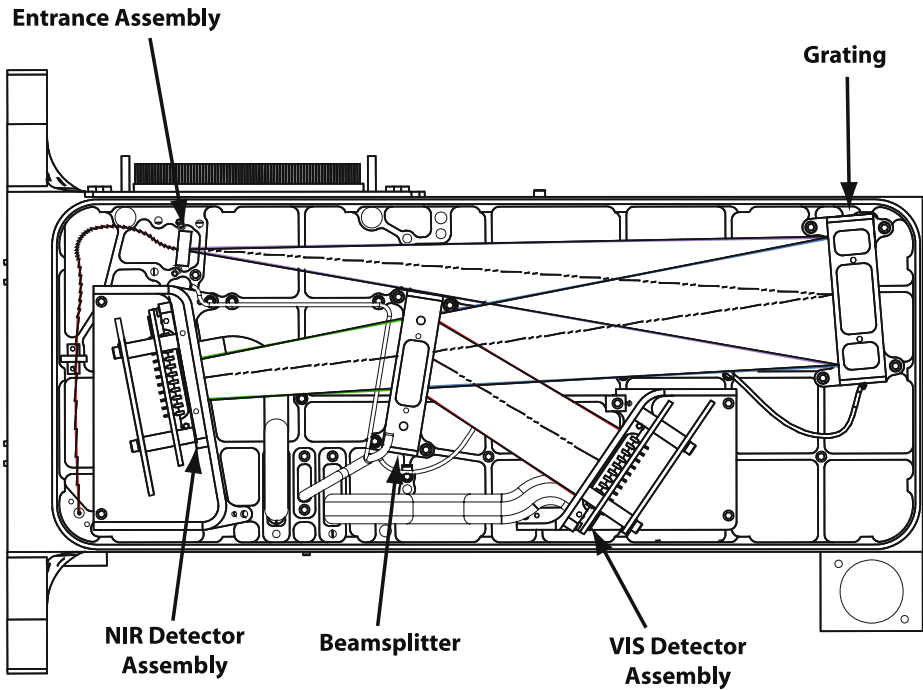
Fig. 17 Solid-model drawing showing the VIRS components

4.5.1 Optical Mechanical Design

Figure 18 shows a cross-section view of the VIRS channel. The fiber feed from the telescope enters through a hole in the floor of the optical bench and is routed to the entrance assembly, which is shown in Fig. 19. Its output end is cemented into a ferrule and clamped to the top of the assembly using a "V" block. The "slip fit" provided by loosening the "V" block retaining screws provides a convenient method for adjusting the focus of the instrument before cover installation. Two grain-of-wheat lamps (not shown in Fig. 19), which are located on either side of the ferrule, provide flat-field illumination for the detectors during calibration. The entrance assembly also supports a shutter mechanism that is used to interleave dark current spectra with normal observations. This is accomplished using an Aeroflex 16305 stepper motor to rotate an arm in front of the fiber input to block the incoming beam. A light-emitting and receiving diode pair provides an electrical signal that indicates when the shutter is closed.
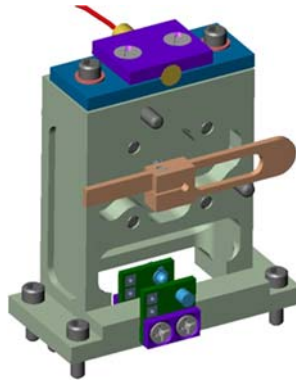
Light diverging from the fiber travels 210.9 mm to the grating vertex, which is rotated 9.08° with respect to the incoming beam. The grating diffracts wavelengths 200–1,500 nm into a 7.5° fan of angles projected toward a flat focal plane, which is located 206 mm from the grating pole and is rotated by 9.1° with respect to its normal.

A 6.1-mm-thick, fused-silica beam splitter, which is rotated by 19° relative to the incident fan, intercepts the rays before they reach the focal plane. The lower half of the first surface reflects all wavelengths toward the visible focal plane where they are imaged onto a Hamamatsu S3901-512SPL negative-channel metal-oxide semiconductor (N-MOS) silicon diode array. The upper half of the first surface transmits light to the second surface of the beam splitter, which has a concave cylindrical surface with a 250-mm vertical radius of curvature. Both the upper half of the first surface and the entire second surface have infrared anti-reflection coatings optimized for wavelengths greater than 900 nm. After light exits the beam splitter it travels to the infrared detector head (NIR) where it traverses a fused silica convex-plano cylindrical lens, which has a 6.6-mm vertical radius of curvature, before being

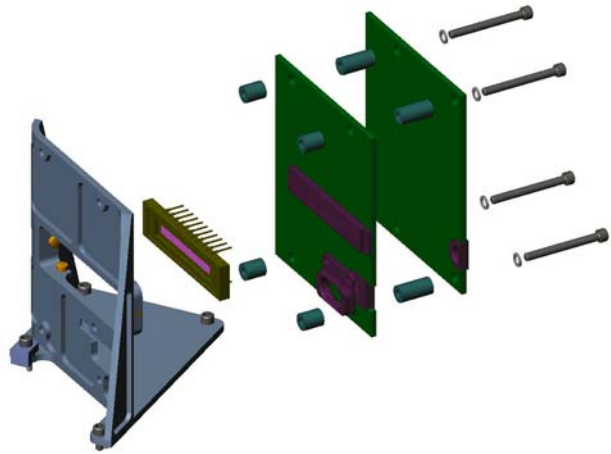**Fig. 18** Cross-section view of the VIRS showing the locations of major components

Fig. 19 VIRS entrance assembly

imaged onto a Hamamatsu G8162-256S InGaAs diode array. The two opposing cylindrical surfaces remove astigmatism from the spectral images in order to focus all the light from the grating onto the detector pixels (see Fig. 8).

4.5.2 Detector Head Assemblies

Figure 20 shows a solid-model view of the VIS detector head. The diode array and its control and readout electronics are mounted on a pair of 75-mm-square printed circuit boards, which are inter-wired and supported in the corners by four aluminum spacers. This arrangement produces a lightweight, compact (75 mm × 75 mm × 50 mm tall) integrated sensor package

Fig. 20 Exploded view of the VIS detector assembly

with a single 15-pin Airborn micro-connector for both power and signal. It is aligned to the detector housing by inserting the diode array package, which is soldered to the front side of the first printed circuit board, into a pocket fitted with Vespel® side pads that contact the diode array package to provide horizontal and vertical registration. Custom-length spacers located between the front surface of the first printed circuit board and the housing determine the distance from the grating to the detector. Socket cap screws, which pass through the centers of the spacers, hold the sensor package in place. This approach, which uses the rigidity of the printed circuit board to maintain focus, is adequate for the VIRS application because the $f/5$ focal ratio of the spectrograph and 0.1-mm-wide imaging footprint allow for up to ± 0.1 mm change in focus with negligible loss of spectral resolution. The mechanical configuration for the NIR detector head is nearly identical to that of VIS except that the cylindrical condensing lens and mount are attached to the front surface of its housing and its mounting footprint modified for placement on the optical bench.

Table 4 summarizes characteristics for both VIS and NIR detectors. Although the mechanical configurations of their two assemblies are nearly identical, there are substantial differences in their architecture and the design of their control and readout electronics. The VIS has a linear array of 512 P–N junction photodiodes that consist of an N-type silicon diffusion layer on a P-type silicon substrate. Photons impinging on a diode are converted into electrons, which are stored in the junction. A simple linear shift register sequentially connects the diodes to an output video line. When a diode is connected to the video line, its charge is transferred to a charge-sensitive amplifier, which is located on board 1 of the sensor assembly along with the array package, and converted to an output voltage that is proportional to the charge accumulated since its last readout. This voltage is transformed into a digital number in a 16-bit analog-to-digital (A/D) converter (ADC), which is located on board 2 of the sensor assembly. After the charge is read out from the diode, it is disconnected from the video line. The readout process automatically resets the diode for its next integration. External clock signals, generated in the FPGA on the Digital Electronics Board

Table 4 VIRS detector characteristics

Parameter	Value	
	VIS channel	NIR channel
Type number	S3901-512SPL	G8162-256S
Photodiode material / substrate	N-silicon on P-silicon	P-InGaAs on N-InGaAs
Format – pixel pitch	512–50 μm	256–50 μm
Pixel height	2,500 μm	500 μm
Saturation charge	3.12×10^8 e$^-$	1.87×10^8 e$^-$
Dark current @ 10°C	3.2×10^5 e$^-$/pixel	9.0×10^6 e$^-$/pixel
Readout noise	5,500 e$^-$	8,900 e$^-$
Readout time	8 ms	4 ms
Digital scale factor	1,190 e$^-$/DN	1,190 e$^-$/DN

(Sect. 4.6), sequence the array readout. For data acquisition the array is first read out twice at a 66.67-kHz per diode rate (7.7 ms total readout time). It is then allowed to collect photo-charge for some integration period before it is sequentially read out at the same 66.67 kHz. This produces a spectrum with a sliding integration time because the first pixel start and stop times are displaced from those of the last by ∼7.7 ms.

The NIR detector has a linear array of 256 P–N junction photodiodes that consist of a P-type InGaAs diffusion layer on an N-type InGaAs substrate. In addition to the diode, each pixel has a sample-and-hold circuit and a charge-to-voltage converter associated with it. This architecture simplifies the design of the external readout electronics and supports si-multaneous integration times because the entire array can be reset with a single control pulse from the FPGA. At the end of the integration period, another control pulse initiates a par-allel transfer of accumulated charges to each pixel sample-and-hold. The voltages from the individual pixels are then read out using a shift register to connect sequentially the outputs of the pixel amplifiers to a video line at a 66.67-kHz rate. Output voltages are transformed to digital numbers using an analog-to-digital converter identical to VIS.

The external timing in the FPGA is designed to maximize the simultaneity with which the two detectors acquire a VIRS spectrum. First the VIS detector is read out twice in succession and the output discarded to reset its pixels. At the end of the second readout, the FPGA issues reset-start integration pulses to the NIR detector. After charge collection is complete, the FPGA issues a stop integration pulse to NIR and initiates a simultaneous readout from both detectors. Because the integrations on the VIS pixels start and stop at slightly different times, they each sample slightly different scenes as the spacecraft moves. During Mercury orbital observations typical integration times are either 1 or 2 s. Simulations done using the MESSENGER spacecraft orbital geometry show that the ∼8 ms time skew between the first and last VIS pixel never introduces more than a 0.5% change in the area of the scene.

4.6 Interface and Control Electronics

The MASCS overall electronics design is shown in Fig. 21. The Low-Voltage Power Sup-ply (LVPS), Event Processing Unit, Digital Electronics Board (DEB), and Breakout Board (BOB) are installed as a stack mounted on the side of the MASCS instrument case. The LVPS, EPU, and DEB are external to the case and are mounted in individual stacking frames. The BOB is mounted to the inside of the case, with its stacking connector passing through
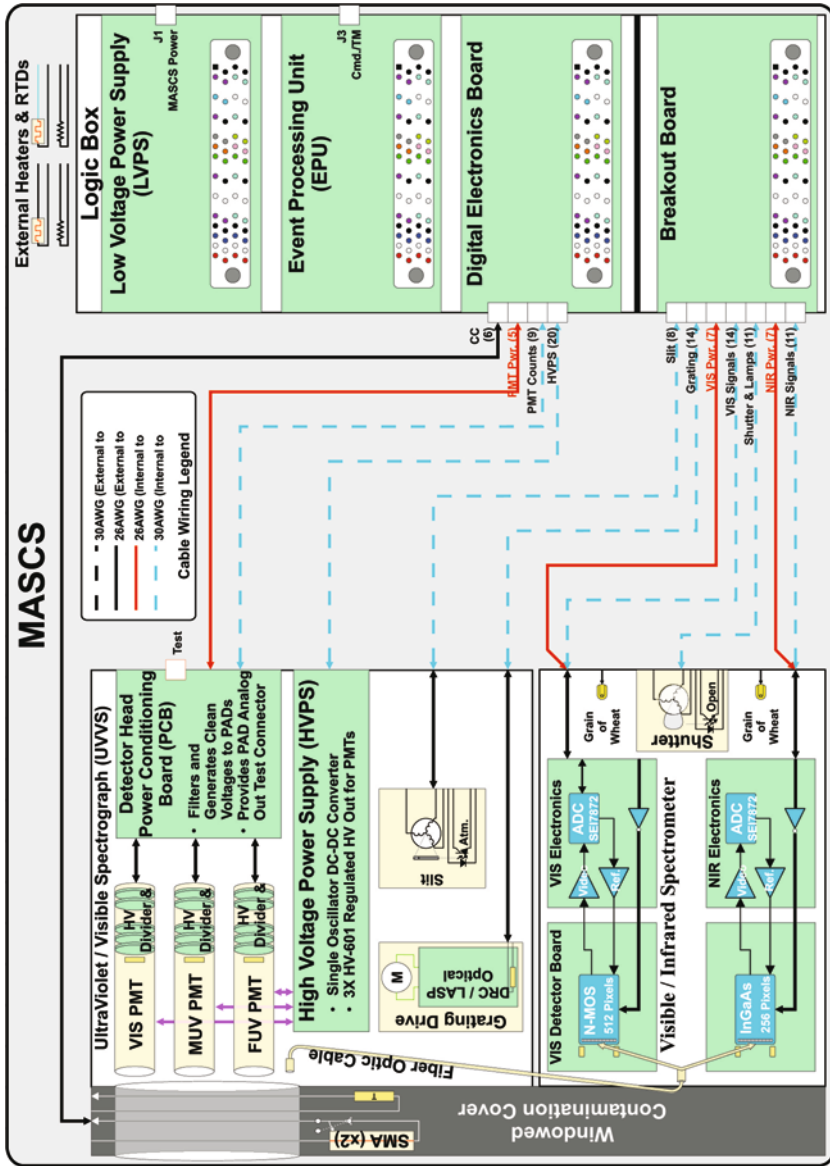
Fig. 21 MASCS electrical block diagram

an opening in the case wall. All board-to-board connections in the stack pass through the 96-pin connectors.

The LVPS and EPU assemblies (Hawkins et al. 2007) were designed and built by The Johns Hopkins University Applied Physics Laboratory (APL). The MASCS team designed the DEB and BOB assemblies to match the APL mechanical and electrical designs, allowing the four boards to stack together. Most of the power dissipation in MASCS occurs on the LVPS, EPU, and DEB. To isolate these heat-producing boards from the optics and sensors, the DEB stacking frame includes a titanium spacer that reduces heat transfer.

The DEB performs many functions in a small space. For the UVVS channel DEB monitors and controls the grating drive, controls PMT integration times, counts PMT pulses during integrations, controls the high-voltage power supply, and controls and monitors the slit mask position. For the VIRS channel DEB controls the array detector integration times, provides clock signals for the detectors, receives and buffers digitized detector data in onboard memory, controls and monitors the shutter, and controls the two flat-field stimulus lamps. DEB includes one FPGA, an Actel RT54SX32S. Three analog-to-digital converters are used for the grating drive A and B signals and for instrument housekeeping data. Additional housekeeping monitors are handled by an ADC on the LVPS board. DEB also controls the pin-puller actuator for the telescope contamination cover and provides external connectors for cabling to the high-voltage power supply, PMT assembly, and contamination cover actuator and temperature sensor.

The BOB provides drivers for the slit mask and shutter mechanism as well as for the grating drive motor. It provides power and data connections for the VIRS VIS and NIR array detectors, and it is the physical location for most of the internal MASCS connectors.
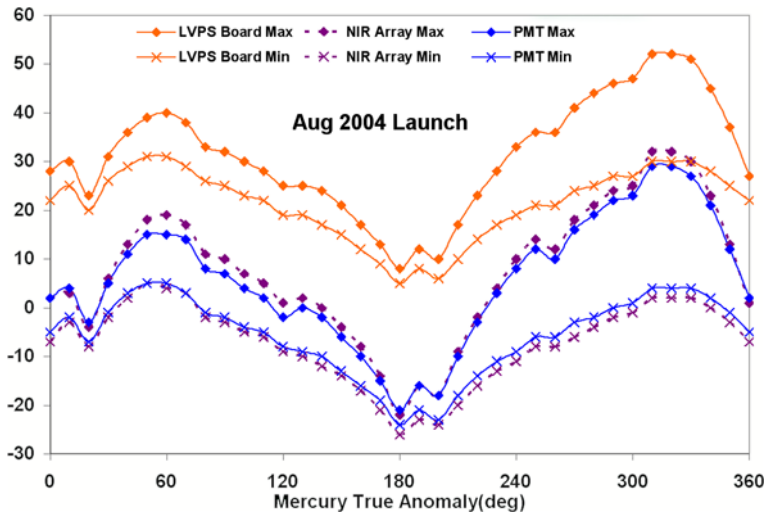
MASCS makes extensive use of "nano" style connectors to save mass and board mounting space. Most cables in the instrument are hard-wired at one end with a connector on the other, again to save mass and space. Nickel-coated aramid fiber braided tubing, which is much lighter than metal braid, is used for cable over-shields where required.

Detector electronics for the UVVS PMTs and the two VIRS array detectors are physically located as close as possible to the sensors to minimize noise on low-level analog signals. Divider chain and PAD electronics are located in a miniaturized five-board stack at the output end of each PMT. A power conditioning board is mounted directly to the ends of the three PMT assemblies with pin-and-socket connections. This board provides conditioned low-voltage power to the PADs and provides the hard-wired termination point for the PMT power and data cable.

Each of the VIRS array detectors is integrated into a two-board electronics assembly that provides the signals required to operate the detector and immediate digitization of the detector output. Each array has two temperature sensors. The NIR array has one internal and one external thermistor. The VIS array has two external thermistors, one at each end of the array.

4.7 Thermal Design

The goal of the thermal design is to maintain a stable, cool temperature for the instrument, particularly the detectors. The only active thermal control components are the redundant survival heaters, which are powered by the spacecraft and controlled by thermostats located near the MASCS center of mass. Titanium spacers under each mounting foot of the instrument thermally isolate MASCS from the spacecraft instrument deck. A titanium spacer also isolates the main electronics stack from the rest of the instrument, minimizing heat transfer into the optics and detectors. Most of the external surfaces of the instrument are treated with

Fig. 22 Predicted MASCS component temperatures during one Mercury year

high-emissivity black paint and are radiatively coupled to the spacecraft payload adapter ring. Protection from the highly varying thermal environment when the spacecraft is in Mercury orbit is provided by a multilayer insulation (MLI) tent that exposes only the end of the instrument that contains the MASCS telescope aperture and contamination cover.

Figure 22 shows the temperatures of critical MASCS components from the instrument thermal model during a single 88-day Mercury year. Two curves for each component show the maximum and minimum temperature over a single 12-hour orbit. For example, at 60° Mercury true anomaly, the LVPS board varies between 42°C and 30°C over an orbit. The lower two curves are the predictions for the detectors indicating that they will operate at 10°C or lower during most of the mission, minimizing their dark current.

4.8 Instrument Software

The MASCS instrument flight software controls all instrument functions, accepts and executes commands, and formats and transmits telemetry for eventual downlink. The software executes on the RTX-2010 processor on the APL-provided EPU that serves as the instrument computer. As with most of the MESSENGER instruments, MASCS makes extensive use of the APL common code for the EPU. Common code functions make up about half of the 56.6-kbyte total size of the program code; MASCS-specific functions make up the other half.

At power-on MASCS runs in boot mode, executing a boot program that was created by APL and delivered in a programmable read-only memory (PROM) with the EPU. The boot program provides basic communications and limited state-of-health monitoring but no science capabilities. From boot mode MASCS is commanded into application mode, in which it has full capabilities. The application-mode program is built as an executable image using source code for both MASCS-specific and common code functions. The application mode program is stored in an electrically erasable programmable read-only memory (EEPROM). New application code can be uploaded and stored in the instrument if in-flight modifications to the program become necessary.

The MASCS software can receive and execute 35 common-code commands and 52 MASCS-specific commands. In normal science operation, most incoming commands are used to configure the UVVS or VIRS for the next observation. Once a UVVS or VIRS scan has started, no further commanding is required until the scan is complete. In general the order in which commands are sent to the instrument is not critical, except that all parameters should be set to their desired values before an observation is started. For actions where the command sequence is important, the software enforces the correct sequence and will reject commands that are sent out of order.

The MASCS software can generate 20 different Consultative Committee on Space Data Systems (CCSDS) telemetry packets. Fifteen of these are status or diagnostic packets. The other five contain science data with a distinct packet type for each MASCS detector. Each MASCS science packet contains sufficient instrument configuration information for identification and analysis of that packet's data. Missing packets from an observation would leave gaps in the data record but would not preclude analysis of the packets that are received.

UVVS science packets contain two data fields in addition to the required CCSDS primary and secondary headers. A configuration data structure contains information that completely describes the instrument's state at the time an observation was performed. A detector data field contains all of the PMT data gathered during the observation. Nominal observation planning must take into account the restriction that all of the data from one observation should fit into a single CCSDS packet. Planned science observations for MASCS fit well within this restriction.

UVVS PMT data are optionally compressed with an algorithm that reduces the 16-bit raw values to 9-bit compressed values, which are then packed end-to-end in the CCSDS packet data field. Compression allows more data values, that is, longer observations, to fit within the one-packet-per-observation constraint. The compression algorithm is a sqrt($2N$) calculation, where N is the raw data number of counts per PMT integration time, originally developed for the Cassini UltraViolet Imaging Spectrograph (UVIS) (Esposito et al. 2004). The square root calculation is a bit-wise successive approximation algorithm that returns a rounded integer result in a deterministic time. It is well suited to a real-time program running on a processor without floating point hardware. Raw data values less than 128 are not compressed, avoiding the relatively large errors that would result from computing their integer square roots. The algorithm is somewhat lossy (less so at higher values) but is a good solution for a photon counting detector.

VIRS science packets also contain two data fields in addition to the required CCSDS primary and secondary headers. As with UVVS packets, a configuration data structure describes the instrument's state at the time an observation was performed. VIRS, however, does not have the constraint that all observation data must fit within a single CCSDS packet. VIRS observation data may span many telemetry packets, though each packet contains enough information to allow successful data analysis even if neighboring packets are missing.

VIRS detector data are optionally compressed in several ways. The VIS and NIR array detectors overlap somewhat in wavelength, and in normal operations MASCS is configured to downlink only the nonoverlapping data from the VIS detector to minimize redundant data. Both VIRS detectors have a physical pixel resolution that exceeds MASCS spectral resolution requirements, so in normal operations MASCS is commanded to bin VIS and NIR data to reduce data volume without degrading the science return. Both of these methods of reducing data volume involve some losses. A third option, usually invoked in addition to the preceding methods, provides a further lossless compression by computing the successive difference of each spectrum within a packet and packing each differenced result in the minimum number of bits.

In general the MASCS instrument design does not require that the software perform fault detection and correction. However, if the VIS PMT views the illuminated surface of Mercury when its high voltage is on, the incoming light level is above its working dynamic range. If this occurs the VIS PMT noise temporarily increases above acceptable levels and will not return to normal until the detector views a dark target for some time. Full recovery can take many minutes. To avoid this problem, software monitors VIS counts whenever the photomultiplier tube high voltage is on. The result is compared against a commandable threshold value; if the value exceeds the threshold software turns off the VIS high voltage.

5 Radiance Conversion and Calibration

Both the UVVS and VIRS measure the radiance arriving at the input aperture of the instrument, and a single equation defines the conversion of instrument output (photomultiplier tube counts, solid-state detector data numbers, and ancillary engineering values) to geophysical data (radiance):

$$L(\lambda_j) = \frac{[C(\lambda_j) \cdot N(C) - D(j) - S_l(\lambda_j)]/\Delta t}{A \cdot \Delta\lambda \cdot R_c(\lambda_j) \cdot FF_j \cdot \overline{\Omega}}. \tag{6}$$

Here, C is either the photomultiplier counts at grating position j or VIRS array data number for pixel j obtained during integration time, Δt. N is the detector linearity correction, which includes analog-to-digital converter errors for the VIRS arrays, and D is the dark count or dark current data number correction. A is the area of the telescope, $\Delta\lambda$ is the spectral bandpass, R_c is the instrument responsivity at the center of the FOV for a detector array with uniform pixel sensitivity, FF is the flat-field correction for the VIRS arrays ($FF = 1$ for the photomultipliers), S_l is the stray plus scattered light correction ($S_l = S_l' + S_{\text{Stray}}$). S_l' is negative for bright spectral features (more light is scattered out of position/pixel j than is scattered in by all other wavelengths), and positive for faint spectral features (less light is scattered out of position/pixel j than is scattered in from all other wavelengths). Stray represents the light that is diffusely scattered from internal instrument surfaces. $\overline{\Omega}(\lambda_j)$ is the instrument-effective FOV (the responsivity averaged over the geometrical FOV divided by R_c).

The signals from UVVS are counts from the photon-counting detectors, and the dark counts are expected to depend weakly on temperature over a MESSENGER orbit. There will be a background signal from telescope scattered light for some limb-drift observations made near apoapsis. This background will be determined by measuring the spectrum for 2–3 steps beyond the parent emission line. VIRS dark current will be measured by periodically closing a shutter located at the entrance to the spectrograph. UVVS detector nonlinearity is caused by the processing dead time in the detector pulse-amplifier-discriminator and is typically 2.5% at 50-kHz count rates. VIRS nonlinearity is caused by well saturation in the array detectors and by differential nonlinearity in the analog-to-digital converter. It is expected to be less than 5%. The scattered light correction appears in the numerator as a value that must be subtracted from observed signal (C) to correct for light scattered from all other wavelengths into position/pixel j: $S_l'(\lambda_j) = A \cdot \Delta\lambda \cdot FF_j \cdot \overline{\Omega} \cdot \int L(\lambda') \cdot R_c(\lambda') \cdot G(\lambda_j - \lambda')d\lambda'$, where G is the grating scatter distribution function, which is often approximated as a Lorentzian profile plus constant background (Woods et al. 1994). Responsivity is the quantum throughput (QT) of the optics and detectors at the center of the FOV, and $\overline{\Omega}(\lambda_j)$ is the effective FOV: $\overline{\Omega}(\lambda_j) = \int R(\lambda_j\theta, \phi)d\Omega/R_c(\lambda_j)$. Radiometric calibrations using radiance standards (irradiance standards and reflectance screens) that fill the instrument aperture and FOV measure

the quantity $\overline{R} = A \cdot \Delta\lambda \cdot R_c(\lambda_j) \cdot FF_j \cdot \overline{\Omega}$. Calibrations using standard detectors and star sources that fill only the aperture measure $A \cdot R_c(\lambda_j) \cdot FF_j$, and $\overline{\Omega}(\lambda_j)$ and $\Delta\lambda$ must be determined separately by scanning the FOV and measuring monochromatic lines, respectively. Prelaunch values for the various parameters appearing in (6) were determined during instrument characterization and calibration using both radiance and source standards (McClintock et al. 2004).

Conversion of exospheric radiance to column emission rate requires knowledge of atomic cross-sections and solar flux, both of which are well known. Surface reflectance is typically calculated by dividing measured radiance at the instrument aperture by solar irradiance that is measured by a separate instrument. This approach can introduce artifacts in the derived reflectance. To mitigate these artifacts, the MESSENGER project made careful measurements of the lunar reflectance with MASCS during an Earth flyby, which occurred in August 2005 (Holsclaw et al. 2005; Bradley et al. 2006). Comparing these data to the Mercury observations will provide an invaluable method for validating MASCS reflectance values derived from the Mercury surface radiances. In-flight measurements of stellar irradiance also provide a technique for routinely tracking values of $A \cdot R_c(\lambda_j) \cdot FF_j$.

6 Observation Scenarios

6.1 Exosphere Measurements

UVVS measures exospheric composition and structure by observing solar radiation that is scattered by atoms above the sunlit surface of Mercury. Its wavelength coverage includes five of six known species (H, O, Na, K, and Ca), excluding only He. Altitude profiles obtained from sequences of mini-scans ($\sim$16 step scans at a cadence of 0.5 s/step) centered on the resonance wavelengths will be used to determine temperature and density. Broad system scans that are executed near apoapsis will be used to map the extended distributions of these species. Observations will also include both mini-scans at resonance wavelengths to search for predicted species that have not been previously detected (e.g., Si, Al, Mg, Fe, S, OH) and broad spectral scans (115–600 nm) to search for new species. Candidate UVVS measurement wavelengths for the various species are summarized in Table 5.
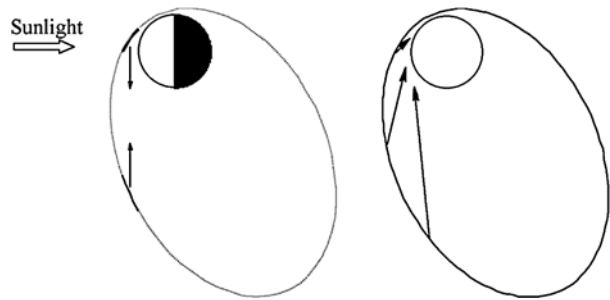
Figure 23 illustrates two examples of UVVS observational geometry. The left panel shows the spacecraft in a noon–midnight obit. In this configuration the UVVS performs a classic limb drift experiment in which the instrument FOV executes an altitude scan above the equatorial limb with a vertical drift rate of $\sim$2 km/sec. Restrictions on spacecraft pointing limit the latitude of the limb tangent point to $\pm15°$. The right panel shows the UVVS

Table 5 Candidate UVVS measurement wavelengths	Species	Wavelength (nm)	Species	Wavelength (nm)
	H (O)	121.6	Na (O)	330.4
	O (O)	130.4	Fe	371.9
	S	181.3	Al	394.4
	Si	252.6	Al	396.2
	Mg	285.1	K (O)	404.4
	OH	308.5	Ca (O)	422.7
	Al	309.2	Na (O)	589.3

O: previously observed species

Fig. 23 UVVS observational geometries for a noon–midnight (*left*) and for a dawn–dusk orbit (*right*)

viewing geometry when the spacecraft is in a dawn–dusk orbit. As the spacecraft rolls about the Mercury–Sun line the UVVS FOV scans the limb. This orbit can be used search for exosphere dawn–dusk asymmetries and to probe high latitudes, particularly in the southern hemisphere.

MASCS is oriented on the spacecraft so that the long axis of the entrance slit is parallel to the limb in the dawn–dusk orbits; therefore, altitude resolution for exospheric observations is $\Delta H = 1.75 \times 10^{-2*}R$ and $\Delta H = 8.73 \times 10^{-4*}R$ for noon–midnight and dawn–dusk orbits respectively, where R is the distance from the spacecraft to the limb tangent point at altitude H.

6.2 Surface Reflectance Measurements

VIRS will measure surface reflectance at visible and near-infrared wavelengths to search for ferrous-bearing minerals (spectral signatures near 1 μm) and Fe-Ti-bearing glasses (spectral signatures near 340 nm). These measurements will be made with a spectral resolution of ∼5 nm per pixel pair and can be binned to lower resolution to reduce data volume. Spacecraft pointing constraints restrict the phase angle ($\Theta = i + e$, where i and e are the incidence and emission angles, respectively) of these to ∼90 ± 15°. The VIRS field of view footprint is $\Delta X = 3.88 \times 10^{-4*}R$. The nominal integration time for VIRS is 1 s; thus the spatial footprint near apoapsis is a 5–6 km rectangle. Near periapsis, the spacecraft orbital motion during an integration period smears the field of view along the spacecraft track by 2–3 km while the cross-track resolution is better than 0.5 km.

UVVS will measure surface reflectance in the 115–300 nm wavelength range and is sensitive to a strong ferrous iron band near 250 nm. It is equipped with a mechanism that replaces the $1° \times 0.04°$ slit by a $0.05° \times 0.04°$ aperture. This aperture is offset from the VIRS entrance aperture by 0.38° in the plane of the UVVS grating dispersion. This arrangement allows VIRS and UVVS to observe the same location on the surface during dawn–dusk orbits by displacing the start of their respective integration times in order to correct for spacecraft ground-track motion.

7 Conclusion

MASCS is one of seven science instruments aboard the MESSENGER spacecraft, which was launched on August 3, 2004, on its way to a one Earth-year orbital mission around Mercury. The instrument contains two spectroscopic channels. UVVS is designed to measure exospheric composition, structure, and temporal variability. VIRS will measure mineralogical composition of the surface. MASCS incorporates innovative approaches to package

proven optical designs and detector technologies into a compact, low-mass instrument that provides a wide range of measurement capability. It will provide important measurements that will address MESSENGER scientific objectives related to Mercury's formation and geologic history and to the composition and transport of volatile species on and near the planet.

References

J.B. Adams, T.B. McCord, *Proc. Apollo 11 Lunar Sci. Conf.*, 1970, pp. 1937–1945

B.A. Anderson et al., Space Sci. Rev. (2007, this issue). doi:10.1007/s11214-007-9246-7

G.B. Andrews et al., Space Sci. Rev. (2007, this issue). doi:10.1007/s11214-007-9272-5

T.A. Bida, R.M. Killen, T.H. Morgan, Nature **404**, 159–161 (2000)

D.T. Blewett, P.G. Lucey, B.R. Hawke, G.G. Ling, M.S. Robinson, Icarus **129**, 217–231 (1997)

D.T. Blewett, P.G. Lucey, B.R. Hawke, Meteorit. Planet. Sci. **37**, 1245–1254 (2002)

E.T. Bradley, G.M. Holsclaw, W.E. McClintock, N.R. Izenberg, Eos Trans. Am. Geophys. Union **87** (Jt. Assem. Suppl.) (2006), abstract P41B-01

A.L. Broadfoot, S. Kumar, M.J.S. Belton, M.B. McElroy, Science **185**, 166–169 (1974a)

A.L. Broadfoot, D.E. Shemansky, S. Kumar, Geophys. Res. Lett. **3**, 577–580 (1974b)

B.J. Butler, D.O. Muhleman, M.A. Slade, J. Geophys. Res. **98**, 15003–15023 (1993)

M.J. Cintala, J. Geophys. Res. **97**, 947–973 (1992)

D.L. Domingue, P.L. Koehn, R.M. Killen, A.L. Sprague, S. Menelaos, A.F. Cheng, E.T. Bradley, W.E. McClintock, Space Sci. Rev. (2007, this issue). doi:10.1007/s11214-007-9260-9

D. Dzurisin, Geophys. Res. Lett. **4**, 383–386 (1977)

L.W. Esposito et al., Space Sci. Rev. **115**, 299–361 (2004)

J.O. Goldsten et al., Space Sci. Rev. (2007, this issue). doi:10.1007/s11214-007-9262-7

S.E. Hawkins III et al., Space Sci. Rev. (2007, this issue). doi:10.1007/s11214-007-9266-3

J.W. Head, C.R. Chapman, D.L. Domingue, S.E. Hawkins, W.E. McClintock, S.L. Murchie, M.S. Robinson, R.G. Strom, T.R. Watters, Space Sci. Rev. (2007, this issue). doi:10.1007/s11214-007-9263-6

G. Holsclaw, T. Bradley, W.E. McClintock, N. Izenberg, R. Vaughan, M.S. Robinson, Eos Trans. Am. Geophys. Union **86** (Fall Meeting Suppl.) (2005), abstract P51A-0896, p. F1198

C.W. Hord et al., Space Sci. Rev. **60**, 503–530 (1992)

D.M. Hunten, T.H. Morgan, D.E. Shemansky, in *Mercury*, ed. by F. Vilas, C.R. Chapman, M.S. Matthews (University of Arizona Press, Tucson, 1988), pp. 562–612

J.F. James, R.S. Sternberg, *The Design of Optical Spectrometers* (Chapman and Hall, London, 1969)

R.M. Killen, A.E. Potter, T.H. Morgan, Icarus **85**, 145–167 (1990)

R.M. Killen, J. Benkoff, T.H. Morgan, Icarus **125**, 195–211 (1997)

R.M. Killen, W.-H. Ip, Rev. Geophys. **37**, 361–406 (1999)

J.C. Leary et al., Space Sci. Rev. (2007, this issue). doi:10.1007/s11214-007-9269-0

P.G. Lucey, Geophys. Res. Lett. **31**, L080701 (2004). doi:10.1029/2003GL019406

P.G. Lucey, D.T. Blewett, B.R. Hawke, J. Geophys. Res. **103**, 3679–3699 (1998)

P.G. Lucey, D.T. Blewett, B.L. Jolliff, J. Geophys. Res. **105**, 20297–20306 (2000a)

P.G. Lucey, D.T. Blewett, G.J. Taylor, B.R. Hawke, J. Geophys. Res. **105**, 20297–20305 (2000b)

S.W. Maymon, S.P. Neeck, J.C. Moody Sr., Soc. Photo-Optical Instr. Eng. **924**, 10–22 (1988)

W.E. McClintock, E.T. Bradley, G.M. Holsclaw, Applied Physics Laboratory Report No. 7384-9470, 2004

M.A. McGrath, R.E. Johnson, L.J. Lanzerotti, Nature **323**, 694–696 (1986)

M. Mendillo, J. Baumgardner, B. Flynn, Geophys. Res. Lett. **18**, 2097–2100 (1991)

T.H. Morgan, R.M. Killen, Planet. Space Sci. **45**, 81–94 (1996)

S.K. Noble, C.M. Pieters, Sol. Syst. Res. **37**, 31–35 (2003)

A.E. Potter, T.H. Morgan, Science **229**, 651–653 (1985)
A.E. Potter, T.H. Morgan, Icarus **67**, 336–340 (1986)
B. Rava, B. Hapke, Icarus **71**, 397–429 (1987)
M.S. Robinson, P.G. Lucey, Science **275**, 197–200 (1997)
M.S. Robinson, G.J. Taylor, Meteorit. Planet. Sci. **36**, 841–847 (2001)
M.A. Slade, B.J. Butler, D.O. Muhleman, Science **258**, 635–640 (1992)
A.L. Sprague, Icarus **84**, 93–105 (1990)
A.L. Sprague, D.M. Hunten, K. Lodders, Icarus **118**, 211–215 (1995)
A.L. Sprague, W.J. Schmitt, R.E. Hill, Icarus **135**, 60–68 (1998)
A.L. Sprague, J.P. Emery, K.L. Donaldson, R.W. Russell, D.K. Lynch, A.L. Mazuk, Meteorit. Planet. Sci. **37**, 1255–1268 (2002)
F. Vilas, Icarus **64**, 133–138 (1985)
J. Warell, D.T. Blewett, Icarus **168**, 257–276 (2004)
J. Warell, A.L. Sprague, J.P. Emery, R.W.H. Kozlowski, A. Long, Icarus **180**, 281–291 (2006)
T.N. Woods, R.T. Wrigley III, G.J. Rottman, R.E. Haring, Appl. Optics **33**, 4273–4285 (1994)